Electronic Supplementary Information

Unexpected long room-temperature phosphorescence lifetimes up to 1.0 s observed in iodinated molecular systems

Junbo Li, [a,b] Xuepu Wang, [b] Yingtong Pan, [b] Yan Sun, [b] Guangming Wang, [b] and Kaka Zhang *[a,b]

[a.] College of Chemistry and Materials Science, Sichuan Normal University, Chengdu 610068, China; [b.] Key Laboratory of Synthetic and Self-Assembly Chemistry for Organic Functional Molecules, Shanghai Institute of Organic Chemistry, University of Chinese Academy of Sciences, Chinese Academy of Sciences, 345 Lingling Road, Shanghai 200032, People's Republic of China.

Email: zhangkaka@sioc.ac.cn

Physical measurements and instrumentation

Nuclear magnetic resonance (NMR) spectra were recorded on a JEOL Fourier-transform NMR spectrometer (400 MHz), including ^{1}H NMR, ^{13}C NMR, ^{19}F NMR and ^{11}B NMR. Mass spectra were performed on Agilent Technologies 5973N and Thermo Fisher Scientific LTQ FT Ultras mass spectrometer. FT-IR spectra were recorded on a Nicolet AVATAR-360 FT-IR spectrophotomerter with a resolution of 4 cm^{-1}. UV-Vis absorption spectra were recorded on a Techcomp UV1050 UV-vis spectrophotometer. Emission spectra were recorded using Edinburgh FLS1000 fluorescence spectrometer, Hitachi FL-7000 fluorescence spectrometer and Horiba FluoroLog-3 fluorescence spectrometer. Photoluminescence quantum yield was measured by a Hamamatsu absolute PL quantum yield measurement system based on a standard protocol (*Adv. Mater.* **1997**, *9*, 230). Photographs and videos were captured by OPPO Reno4 and HUAWEI P30 cameras. Before the capture, samples were irradiated by a 365 nm UV lamp (5 W) for approximately 5 s at a distance of approximately 15 cm. Single-crystal X-ray diffraction analysis was performed on a D8 VENTURE SC-XRD instrument. The X-ray crystallographic data for HBF_2 and IBF_2 has been deposited at the Cambridge Crystallographic Data Centre (CCDC), under the deposition number CCDC 2092212 (data_d8v21153), 2092213 (data_mo_d8v20839_0m), respectively.

TD-DFT calculations

TD-DFT calculations were carried out on ORCA 4.2.1 program with B3LYP functional and def2-TZVP(-f) basis set. The optimized geometry of IBF_2 ground state was obtained by a DFT calculation from single-crystal structure using B3LYP functional and def2-TZVP(-f) basis set. Spin-orbit coupling (SOC) matrix elements between the singlet excited states and triplet excited states were calculated with spin-orbit mean-field (SOMF) methods. The obtained electronic structures were analyzed by Multiwfn software. All isosurface maps to show the electron

distribution and electronic transitions were rendered by Visual Molecular Dynamics (VMD) software based on the exported files from Multiwfn (F. Neese, *Wiley Interdiscip. Rev.: Comput. Mol. Sci.* **2018**, *8*, 1327-1332; A. D. Becke, *Phys. Rev. A* **1988**, *38*, 3098-3100; C. Lee, W. Yang, R. G. Parr, *Phys. Rev. B* **1988**, *37*, 785-789; B. Miehlich, A. Savin, H. Stoll, H. Preuss, *Chem. Phys. Lett.* **1989**, *157*, 200-206; F. Weigend, R. Ahlrichs, *Phys. Chem. Chem. Phys.* **2005**, *7*, 3297-3305; T. Lu, F. Chen, *J. Comput. Chem.* **2012**, *33*, 580-592; W. Humphrey, A. Dalke, K. Schulten, *J. Mol. Graphics* **1996**, *14*, 33-38).

Synthesis of HBF_2 via cascade reaction

Into a round bottom flask was added 0.36 mL acetophenone (3.0 mmol), 4.00 mL acetic anhydride and 1.20 mL boron trifluoride diethyl etherate (9.5 mmol). The reaction mixture was heated to 70 °C for 2 h. After cooling to room temperature, the reaction mixture was extracted with dichloromethane and washed with deionized water. The obtained crude product in dichloromethane was dried over anhydrous sodium sulphate, condensed by rotary evaporation, and then purified by column chromatography over silica gel using the petroleum ether/ dichloromethane (1/1, v/v) as eluent to give 520 mg pale yellow solids with an isolation yield of 82.5%. The HBF_2 was further purified by three cycles of recrystallization in spectroscopic grade dichloromethane/hexane. Single crystal of HBF_2 was grown from dichloromethane/hexane. ^{1}H NMR (400 MHz, Chloroform-*d*, 298K, relative to Me_4Si /ppm) δ 8.09 – 8.04 (m, 2H), 7.73 – 7.66 (m, 1H), 7.54 (t, *J* = 7.9 Hz, 2H), 6.58 (s, 1H), 2.43 (s, 3H). $^{13}C\{^1H\}$ NMR (101 MHz, Chloroform-*d*) δ 192.61, 182.93, 135.49, 131.20, 129.20, 129.03, 97.45, 24.80. $^{19}F\{^1H\}$ NMR (376 MHz, Chloroform-*d*, 298 K, relative to $CFCl_3$ /ppm) δ -139.17 (19.6%), -139.23 (80.4%). $^{11}B\{^1H\}$ NMR (128 MHz, Chloroform-*d*, 298 K, relative to $BF_3{\cdot}OEt_2$ /ppm) δ 0.05. LRMS, m/z 209. HRMS (positive EI) m/z found (calcd for $C_{10}H_9O_2{}^{10}BF_2$): 209.0690 (209.0694).

Synthesis of FBF_2 via cascade reaction

Into a round bottom flask was added 0.21 mL 4-fluoroacetophenone (2.0 mmol), 2.00 mL acetic anhydride and 0.80 mL boron trifluoride diethyl etherate (6.3 mmol). The reaction mixture was heated to 70 °C for 2 h. After cooling to room temperature, the reaction mixture was extracted with dichloromethane and washed with deionized water. The obtained crude product in dichloromethane was dried over anhydrous sodium sulphate, condensed by rotary evaporation, and then purified by column chromatography over silica gel using the petroleum ether/ dichloromethane (1/1, v/v) as eluent to give 315 mg solids with an isolation yield of 69.1%. The FBF_2 was further purified by three cycles of recrystallization in spectroscopic grade dichloromethane/hexane. ^{1}H NMR (400 MHz, Chloroform-*d*, 298K, relative to Me_4Si /ppm) δ 8.15 – 8.07 (m, 2H), 7.25 – 7.19 (m, 2H), 6.53 (s, 1H), 2.43 (s, 3H). $^{13}C\{^1H\}$ NMR (101 MHz, Chloroform-*d*) δ 192.81, 181.57, 168.61, 166.02, 131.96, 131.87, 127.55, 116.89, 116.67, 97.24, 24.91. $^{19}F\{^1H\}$ NMR (376 MHz, Chloroform-*d*, 298 K, relative to $CFCl_3$ /ppm) δ -100.36; -139.20 (19.8%), -139.26 (80.2%). $^{11}B\{^1H\}$ NMR (128 MHz, Chloroform-*d*, 298 K, relative to $BF_3{\cdot}OEt_2$ /ppm) δ 0.01. LRMS, m/z 228. HRMS (positive EI) m/z found (calcd for $C_{10}H_8O_2{}^{10}BF_3$): 227.0597 (227.0600).

Synthesis of $ClBF_2$ via cascade reaction

Into a round bottom flask was added 0.13 mL 4-chloroacetophenone (1.0 mmol), 2.00 mL acetic anhydride and 0.40 mL boron trifluoride diethyl etherate (3.2 mmol). The reaction mixture was heated to 70 °C for 2 h. After cooling to room temperature, the reaction mixture was extracted with dichloromethane and washed with deionized water. The obtained crude product in dichloromethane was dried over anhydrous sodium sulphate, condensed by rotary evaporation, and then purified by column chromatography over silica gel using the petroleum ether/ dichloromethane (1/1, v/v) as eluent to give 172 mg solids with an isolation yield of 70.5%. The $ClBF_2$ was further purified by three cycles of recrystallization in spectroscopic grade dichloromethane/hexane. ^{1}H NMR (400 MHz, Chloroform-*d*, 298K, relative to Me_4Si /ppm) δ 8.03 – 7.97 (m, 2H), 7.55 – 7.49 (m, 2H), 6.54 (s, 1H), 2.44 (s, 3H). $^{13}C\{^1H\}$ NMR (101 MHz, Chloroform-*d*) δ 193.31, 181.62, 142.32, 130.32, 129.75, 129.70, 97.47, 24.99. $^{19}F\{^1H\}$ NMR (376 MHz, Chloroform-*d*, 298 K, relative to $CFCl_3$ /ppm) δ -139.00 (19.8%), -139.06 (80.2%). $^{11}B\{^1H\}$ NMR (128 MHz, Chloroform-*d*, 298 K, relative to $BF_3{\cdot}OEt_2$ /ppm) δ 0.02. LRMS, m/z 244. HRMS (positive EI) m/z found (calcd for $C_{10}H_8O_2{}^{10}BClF_2$): 243.0299 (243.0305).

Synthesis of $BrBF_2$ via cascade reaction

Into a round bottom flask was added 600 mg 4-bromoacetophenone (3.0 mmol), 4.00 mL acetic anhydride and 1.20 mL boron trifluoride diethyl etherate (9.5 mmol). The reaction mixture was heated to 70 °C for 2 h. After cooling to room temperature, the reaction mixture was extracted with dichloromethane and washed with deionized water. The obtained crude product in dichloromethane was dried over anhydrous sodium sulphate, condensed by rotary evaporation, and then purified by column chromatography over silica gel using the petroleum ether/ dichloromethane (1/1, v/v) as eluent to give 690 mg yellow solids with an isolation yield of 79.6%. The $BrBF_2$ was further purified by three cycles of recrystallization in spectroscopic grade dichloromethane/hexane. ^{1}H NMR (400 MHz, Chloroform-*d*, 298K, relative to Me_4Si /ppm) δ 7.94 – 7.89 (m, 2H), 7.71 – 7.66 (m, 2H), 6.54 (s, 1H), 2.43 (s, 3H). $^{13}C\{^1H\}$ NMR (101 MHz, Acetone-d_6) δ 196.02, 181.88, 133.57, 131.47, 131.42, 130.97, 98.86, 24.90. $^{19}F\{^1H\}$ NMR (376 MHz, Chloroform-*d*, 298 K, relative to $CFCl_3$ /ppm) δ -138.93 (19.9%), -138.99 (80.1%). $^{11}B\{^1H\}$ NMR (128 MHz, Chloroform-*d*, 298 K, relative to $BF_3{\cdot}OEt_2$ /ppm) δ 0.01. FT-IR (KBr, cm^{-1}): ν 3139.8, 3102.3, 1591.4, 1536.6, 1489.1, 1441.3, 1404.8, 1369.5, 1350.2, 1302.9, 1279.8, 1199.5, 1182.0, 1153.4, 1120.8, 1107.3, 1091.0, 1057.8, 1006.5, 977.2, 873.3, 843.9, 828.5, 806.8, 775.5, 741.5, 687.9, 582.9, 490.7, 469.0, 417.8. LRMS, m/z 288. HRMS (positive EI) m/z found (calcd for $C_{10}H_8O_2{}^{10}BBrF_2$): 286.9795 (286.9800).

Synthesis of IBF_2 via cascade reaction

Into a round bottom flask was added 492 mg 4-iodoacetophenone (2.0 mmol), 3.00 mL acetic anhydride and 0.80 mL boron trifluoride diethyl etherate (6.3 mmol). The reaction mixture was heated to 70 °C for 2 h. After cooling to room temperature, the reaction mixture was extracted with dichloromethane and washed with deionized water. The obtained crude product in dichloromethane was dried over anhydrous sodium sulphate, condensed by rotary evaporation, and then purified by column chromatography over silica gel using the petroleum ether/

dichloromethane (1/1, v/v) as eluent to give 480 mg yellow solids with an isolation yield of 71.5%. The IBF_2 was further purified by three cycles of recrystallization in spectroscopic grade dichloromethane/hexane. Single crystal of IBF_2 was grown from dichloromethane/hexane. ^{1}H NMR (400 MHz, Chloroform-*d*, 298K, relative to Me_4Si /ppm) δ 7.91 (d, J = 9.0 Hz, 2H), 7.77 – 7.72 (m, 2H), 6.54 (s, 1H), 2.43 (s, 3H). $^{13}C\{^{1}H\}$ NMR (101 MHz, Chloroform-*d*) δ 193.31, 181.95, 138.65, 130.60, 129.95, 104.15, 97.34, 24.94.$^{19}F\{^{1}H\}$ NMR (376 MHz, Chloroform-*d*, 298 K, relative to $CFCl_3$ /ppm) δ -138.95 (20.7%), -138.99 (79.3%). $^{11}B\{^{1}H\}$ NMR (128 MHz, Chloroform-*d*, 298 K, relative to $BF_3{\cdot}OEt_2$ /ppm) δ 0.01. FT-IR (KBr, cm-1): ν 3132.5, 3092.9, 1586.3, 1576.3, 1532.5, 1482.8, 1439.0, 1402.1, 1366.0, 1349.0, 1304.8, 1276.8, 1199.9, 1187.2, 1150.6, 1122.0, 1107.5, 1088.0, 1054.6, 1003.4, 976.5, 961.4, 872.6, 849.5, 834.6, 810.5, 775.3, 741.9, 688.8, 671.8, 581.0, 489.8, 464.6. LRMS, m/z 336. HRMS (positive EI) m/z found (calcd for $C_{10}H_8O_2{}^{10}BF_2I$): 334.9663 (334.9661).

Supporting Texts

Text S1. In the reported studies, iodinated BF_2bdk compounds have also been synthesized and used for the fabrication of room-temperature phosphorescence materials. For example, the iodinated BF_2bdk in the reported study (*J. Phys. Chem. A* 2017, **121**, 8652) possess similar functional groups but different conjugation lengths when compared to the present iodinated BF_2bdk compounds. We understand that subtle change of molecular structures may lead to drastic change of photophysical studies in the research area of room-temperature phosphorescence materials. The present study achieves room-temperature phosphorescence lifetimes up to 1.0 s in IBF_2-PhB-0.05% samples, whereas phosphorescence lifetimes around 1.0 ms have been observed in the reported study (*J. Phys. Chem. A* 2017, **121**, 8652). Therefore, the present study is different from the reported study (*J. Phys. Chem. A* 2017, **121**, 8652) in both molecular structures and photophysical properties.

Text S2. The photoluminescence quantum yields, rather than phosphorescence quantum yields, of HBF_2-PhB-0.05% and IBF_2-PhB-0.05% are determined to be 9.6% and 9.2%, respectively. The phosphorescence quantum yields should be lower than these values, but an accurate estimation of phosphorescence quantum yields for the present system would be difficult because of the overlap of fluorescence bands and phosphorescence bands. Despite of these, the afterglow brightness and duration of IBF_2-PhB-0.05% samples is still significant because of their long emission lifetimes.

Text S3. With reference to the reported studies (*J. Am. Chem. Soc.*, 2007, **129**, 8942), the double-exponential decay of the fluorescence can be caused by the heterogeneous microenvironments in the solid samples. For the triple-exponential decay of IBF_2-PhB-0.05% samples, the τ_1 part (17.4 ms, 1.0%) can be assigned as fluorescence decay; similar to the reported studies (*Nat. Commun.* 2020, **11**, 842; *Chem. Lett.* 2019, **48**, 126), the fluorescence lifetimes measured by microsecond flash lamp have been found to be in microsecond and even millisecond regimes. The τ_2 part (246 ms, 8.0%) and τ_3 part (1046 ms, 91%) can be attributed to the phosphorescence from IBF_2 triplet excited states in the heterogeneous solid microenvironments. The fluorescence lifetimes of $ClBF_2$-PhB-0.05%, $BrBF_2$-PhB-0.05% and IBF_2-PhB-0.05% samples are shorter than those of HBF_2-PhB-0.05% and FBF_2-PhB-0.05% samples (Table 1). For XBF_2-PhB-0.05% samples (X = Cl, Br, I), the fluorescence lifetimes follow the order of Cl > Br > I, which is in line with the heavy atom effect in organic phosphorescence systems.

Text S4. Donor-acceptor pairs that show intermolecular charge transfer properties have been reported to show excellent afterglow behaviors (*Nature* 2017, **550**, 384), which is caused by the retarded charge recombination between photo-generated radical cations and radical anions in solid matrices. PhB matrices have low-lying HOMOs and high-lying LUMOs, so intermolecular charge transfer between PhB and IBF_2 is insignificant and thus the donor-acceptor afterglow mechanism can be ruled out in the present study.

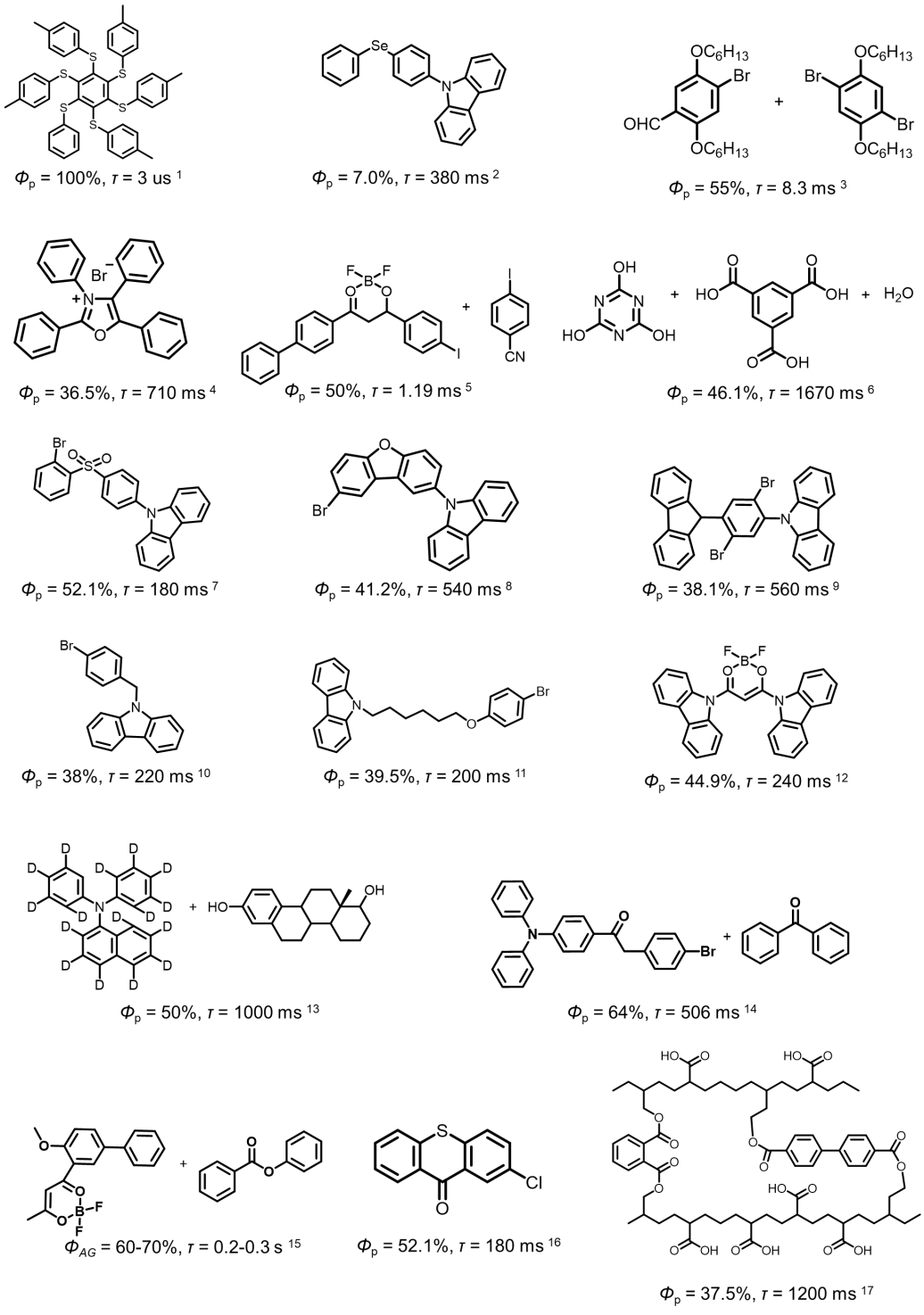

Figure S1. Selected room-temperature phosphorescence organic systems that contain heavy atoms and show long phosphorescence lifetimes, as well as room-temperature phosphorescence and afterglow systems with emission lifetimes around 1.0 s.[1-60] At ambient conditions, we have not found any iodine containing phosphorescence systems that possess emission lifetimes up to 1.0 s, neither in single-component systems nor in dopant-matrix systems at low doping concentrations. Therefore, at room temperature, when doped in PhB matrices at 0.05 wt%, the present IBF_2 molecules possess 38 wt% iodine substituents but show such a long τ_P up to 1.0 s in the dopant-matrix systems; this is an unexpected observation.

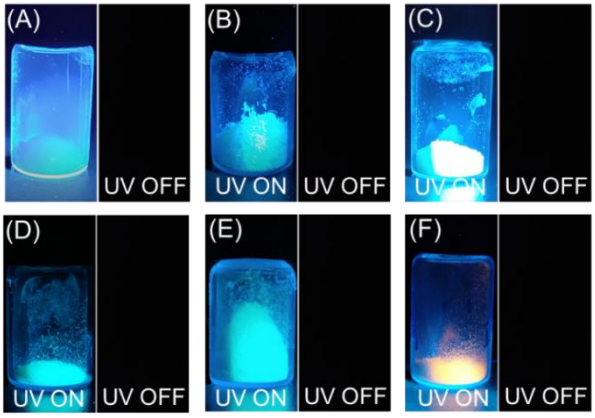

Figure S2. Photographs of (A) phenyl benzoate (PhB) powders and (B-F) BF_2bdk powders (B, HBF_2; C, FBF_2; D, $ClBF_2$; E, $BrBF_2$; F, IBF_2) at room temperature under 365 nm UV light and after removal of 365 nm UV light.

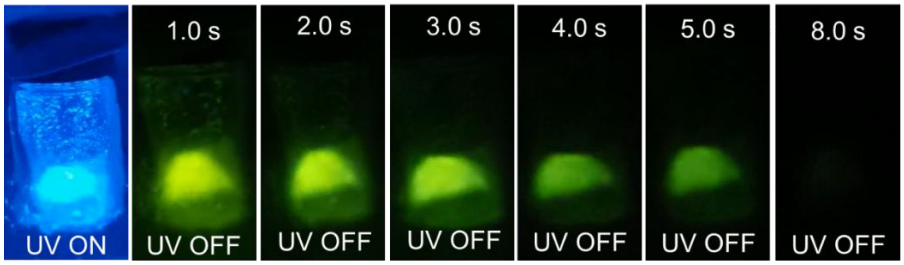

Figure S3. Photographs of HBF_2 powders at 77 K under 365 nm UV light and after removal of 365 nm UV light.

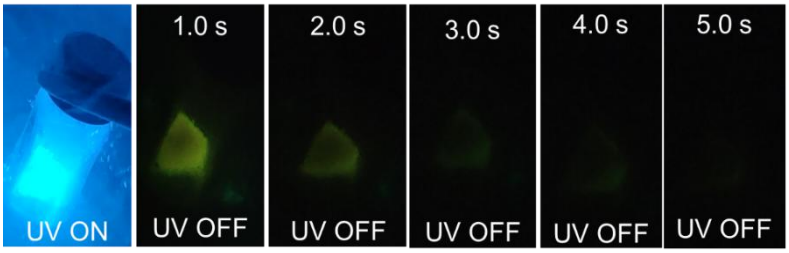

Figure S4. Photographs of FBF_2 powders at 77 K under 365 nm UV light and after removal of 365 nm UV light.

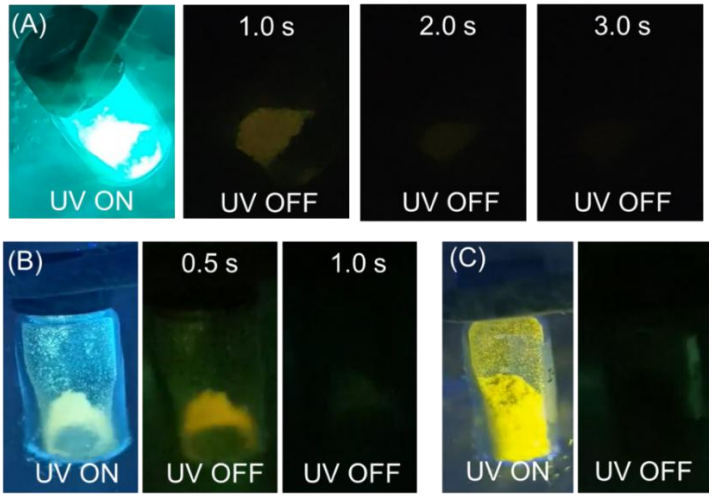

Figure S5. Photographs of (A) $ClBF_2$, (B) $BrBF_2$ and (C) IBF_2 powders at 77 K under 365 nm UV light and after removal of 365 nm UV light.

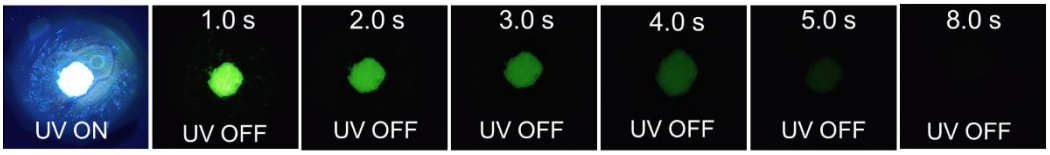

Figure S6. Photographs of IBF_2-PhB-0.05% afterglow powders independently prepared by Yingtong Pan (a coauthor of this manuscript) under 365 nm UV light and after removal of 365 nm UV light. The IBF_2 compound used here was also independently synthesized by Yingtong Pan.

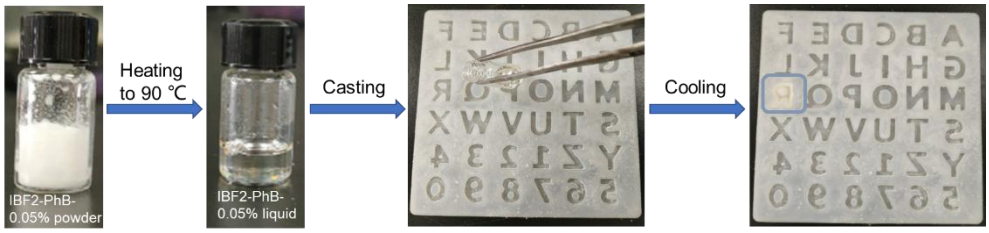

Figure S7. The process of preparing afterglow objects of IBF_2-PhB-0.05% by melt casting with the aid of silicone molds.

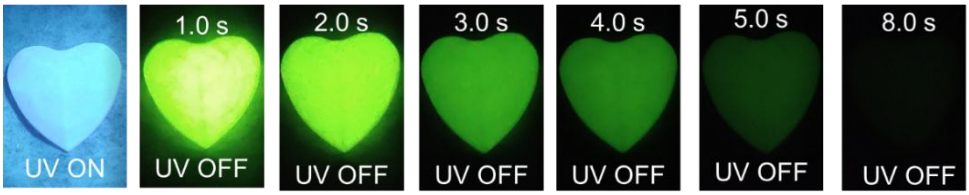

Figure S8. Photographs of the melt-cast heart-shaped object of IBF_2-PhB-0.05% under 365 nm UV light and after removal of the UV light.

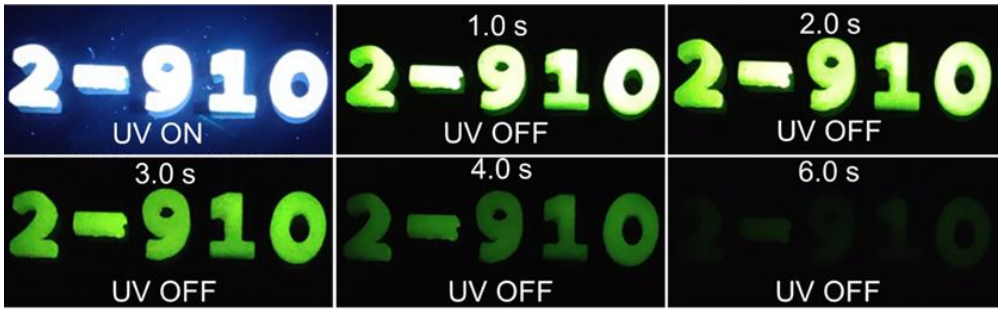

Figure S9. Photographs of the melt-cast object of IBF_2-PhB-0.05% that show our lab room number under 365 nm UV light and after removal of the UV light.

Figure S10. Photographs of phenyl benzoate (PhB) powders at 77 K under 365 nm UV light and after removal of 365 nm UV light. At 77 K, no visible afterglow has been observed for the PhB powders. This observation, together with their molecular structures, suggests that PhB matrices possess high T_1 levels.

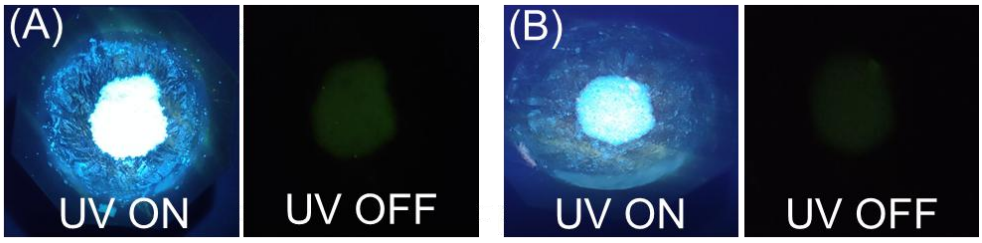

Figure S11. Photographs of (A) IBF_2-BP-0.05% and (B) IBF_2-benzanilide-0.05% powders under 365 nm UV light and after removal of 365 nm UV light.

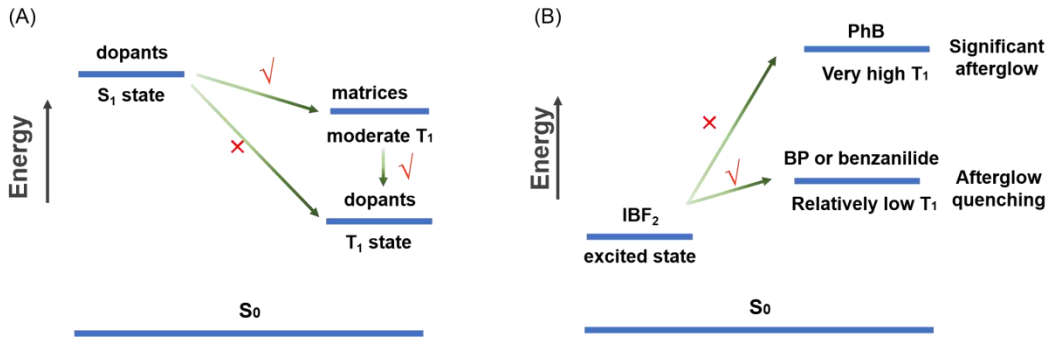

Figure S12. (A-B) The role of organic matrices reported in recent dopant-matrix afterglow systems (A) and in the present afterglow system (B). It has been reported in recent studies that the triplet excited states of organic matrices with energy levels sandwiched between the S_1 and T_1 levels of luminescent dopants can mediate the singlet-to-triplet intersystem crossing of the luminescent dopants, leading to the room-temperature organic afterglow (*Angew. Chem. Int. Ed.* 2020, **59**, 16054; *Nature Commun.* 2021, **12**, 3522). This mediation of intersystem crossing is not the case in the present study since the T_1 level of PhB matrices is higher than both the singlet and triplet excited states of IBF_2 molecules. Actually, the high T_1 level of PhB matrices is very important in the present study to avoid the triplet-to-triplet energy transfer from IBF_2 triplets to the triplet excited states of organic matrices. As discussed in the manuscript, when benzophenone and benzanilide matrices with lower T_1 levels were used as organic matrices, the obtained IBF_2-benzophenone-0.05% and IBF_2-benzanilide-0.05% samples show insignificant room-temperature afterglow; the afterglow quenching is caused by the triplet-to-triplet excited energy transfer from IBF_2 triplet excited states to benzophenone and benzanilide triplet excited states. These observations and analyses receive support from the reported studies by Adachi and coworkers on dopant-matrix systems (*Adv. Funct. Mater.* 2013, **23**, 3386). For the BF_2bkd-matrix systems, it is found that, in our previous studies (*Adv. Optical Mater.* 2021, 2100353; *Angew. Chem. Int. Ed.* 2021, **60**, 17138), the organic matrices with carbonyl functional groups can perturb and interact with the excited states of the luminescent dopants via dipole-dipole interaction, reduce ΔE_{ST}, and thus enhance intersystem crossing of the luminescent dopants, leading to the emergency of organic afterglow properties; this is our understanding on the role of organic matrices in the present dopant-matrix system. Besides, the rigid microenvironments provided by PhB organic matrices can also restrict the nonradiative deactivation of IBF_2 triplet excited states and protect the triplet excited states from oxygen quenching.

Figure S13. Photographs of (A) HBF_2-PhB-0.05%, (B) FBF_2-PhB-0.05% and (C) $ClBF_2$-PhB-0.05% afterglow powders under 365 nm UV light and after removal of 365 nm UV light.

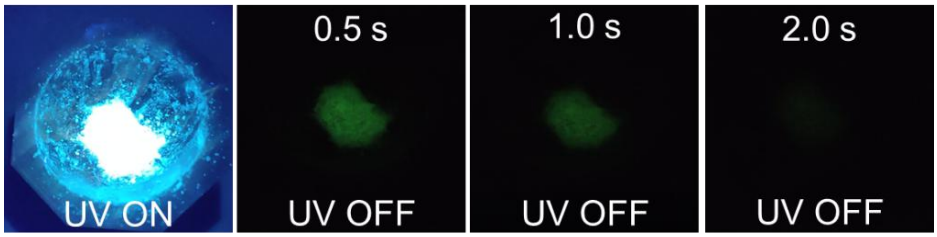

Figure S14. Photographs of $BrBF_2$-PhB-0.05% afterglow powders under 365 nm UV light and after removal of 365 nm UV light.

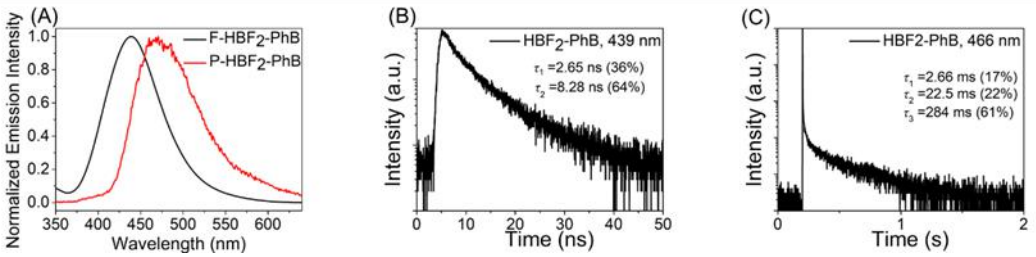

Figure S15. (A) Room-temperature fluorescence and phosphorescence spectra of HBF_2-PhB-0.05% powders. The phosphorescence spectra of HBF_2-PhB-0.05% powders show single peak at 466 nm. (B) Room-temperature fluorescence decay of HBF_2-PhB-0.05% monitored at 439 nm. (C) Room-temperature phosphorescence decay of HBF_2-PhB-0.05% monitored 466 nm.

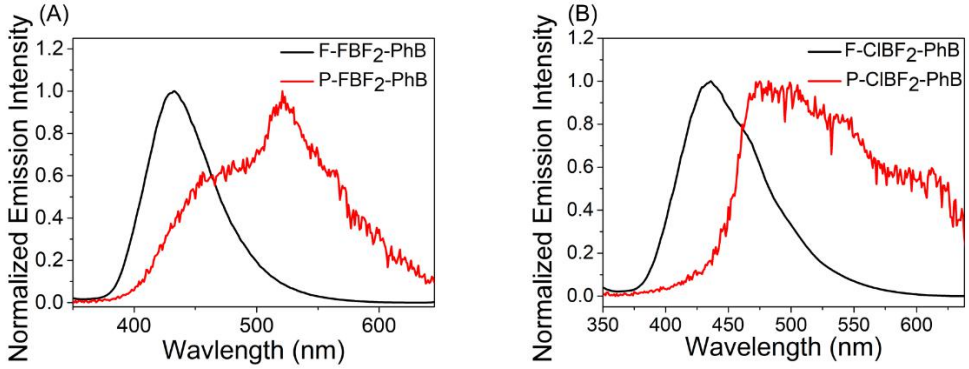

Figure S16. Room-temperature fluorescence and phosphorescence spectra of (A) FBF_2-PhB-0.05% and (B) $ClBF_2$-PhB-0.05% powders. The phosphorescence spectra of FBF_2-PhB-0.05% and $ClBF_2$-PhB-0.05% powders are noisy. The phosphorescence decay of FBF_2-PhB-0.05% and $ClBF_2$-PhB-0.05% powders monitored at 521 nm and 500 nm, respectively, have also been measured to show insignificant signals (data not shown). Therefore, we didn't give further interpretation on these noisy phosphorescence spectra and the very weak phosphorescence signals.

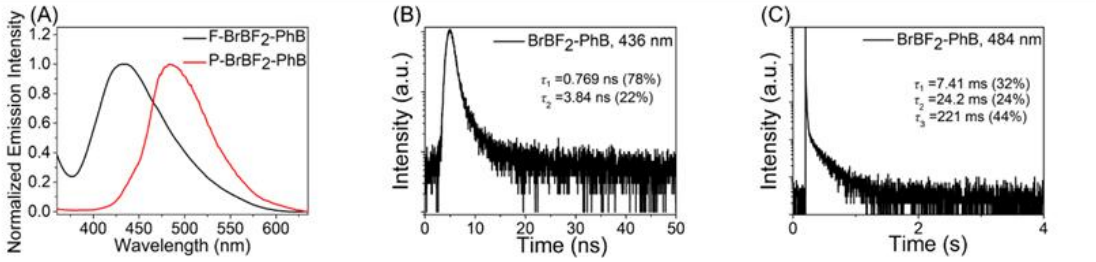

Figure S17. (A) Room-temperature fluorescence and phosphorescence spectra of $BrBF_2$-PhB-0.05% powders. (B) Room-temperature fluorescence decay of $BrBF_2$-PhB-0.05% monitored at 436 nm. (C) Room-temperature phosphorescence decay of $BrBF_2$-PhB-0.05% monitored 484 nm.

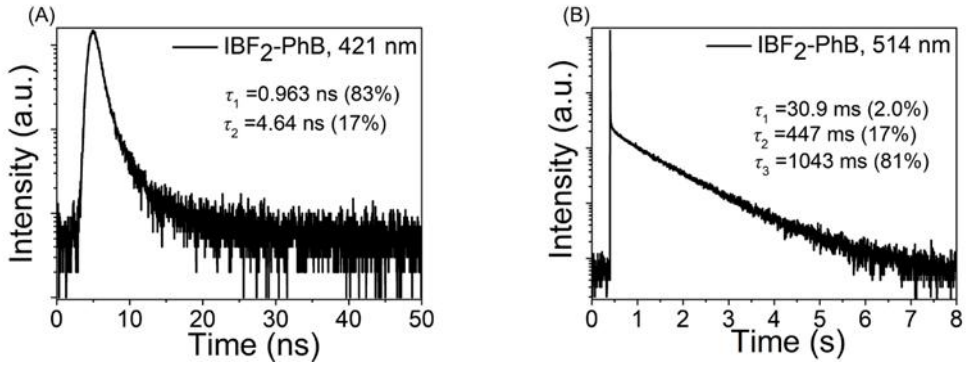

Figure S18. (A) Room-temperature fluorescence decay of IBF_2-PhB-0.05% monitored at 421 nm. (B) Room-temperature phosphorescence decay of IBF_2-PhB-0.05% monitored at 514 nm. This is also a repeated experiment that starts from material preparation and phosphorescence lifetime measurements. In this repeated experiment, a new IBF_2-PhB-0.05% sample was prepared to show afterglow properties and then the phosphorescence decay profile of this sample was recorded.

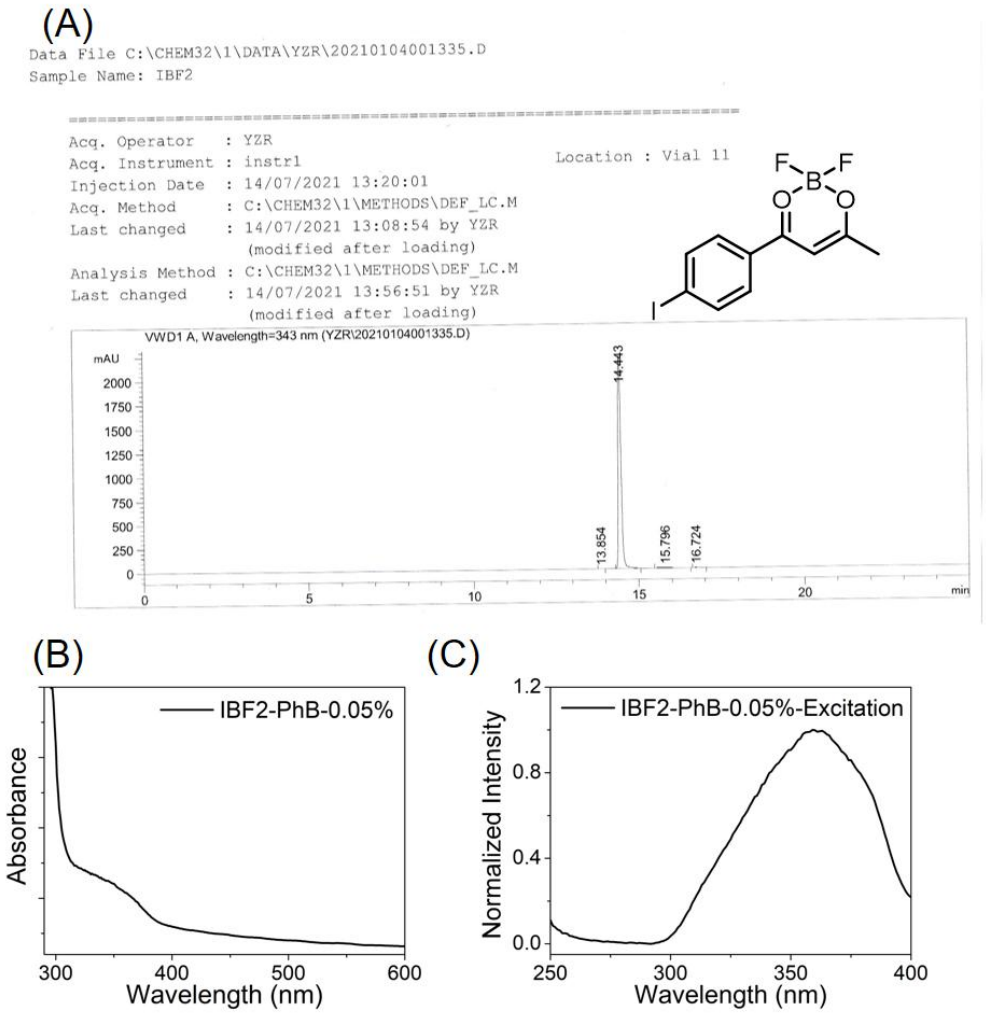

Figure S19. (A) HPLC results of the IBF_2 compound. (B) UV-Vis spectra and (C) excitation spectra of IBF_2-PhB-0.05% afterglow materials. In the present study, the IBF_2 compounds are purified by careful column chromatography followed by three cycles of recrystallization in spectroscopic grade dichloromethane/hexane. HPLC results show that the IBF_2 compounds possess high purity. It has been reported that isomeric impurity mechanism (*Nat. Mater.* 2021, **20**, 175) can lead to the emergency of room-temperature organic afterglow in carbazole systems. Retarded charge recombination between photo-generated radical cations and radical anions is responsible for the room-temperature afterglow behaviors. In the present study, IBF_2 powders alone show no room-temperature afterglow. For the IBF_2-PhB-0.05% afterglow materials at such a low doping concentration, since the IBF_2 molecules and the possible impurities are well separated by PhB matrices, charge separation and recombination processes between IBF_2 molecules and the possible impurities are statistically negligible. If the possible impurities show afterglow properties after doping into PhB matrices, the afterglow emission intensity would be very weak because the doping concentration of the possible impurities in organic matrices is very low (1 ppm or even lower). The above experiments and analyses can rule out the possibility that the room-temperature afterglow is originated from some impurities. The excitation spectra of IBF_2-PhB-0.05% samples have been found to show peaks with similar wavelengths as their UV-vis absorption spectra Therefore, the afterglow properties of IBF_2-PhB-0.05% samples can be exclusively attributed to the phosphorescence decay of IBF_2 molecules dispersed in PhB matrices.

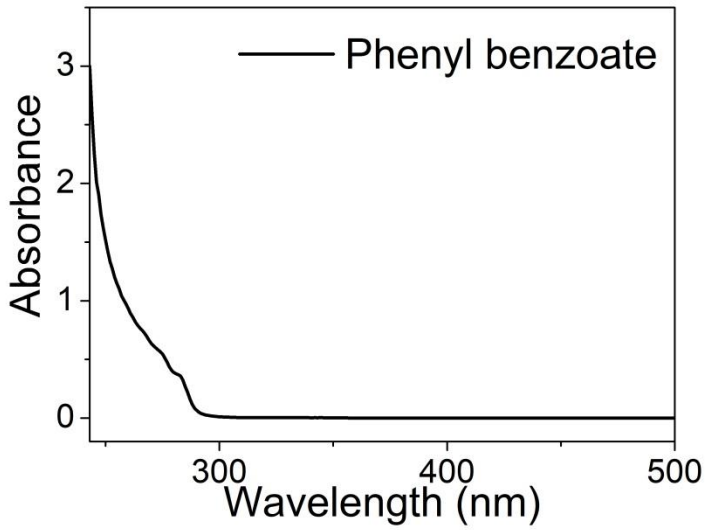

Figure S20. UV-Vis spectra of the melt-cast film of phenyl benzoate matrices. In the literature, triplet-to-triplet excited state energy transfer from organic matrices to luminescent dopants has also been reported to give rise to organic afterglow behaviors in two-component systems (*CCS Chem.* 2020, **2**, 1391). In these studies, efficient afterglow properties can only be observed when the organic matrices are well excited. The PhB matrices show negligible UV-vis absorption at 365 nm or longer wavelengths. The present IBF_2-PhB-0.05% samples can be excited at 365 nm UV to exhibit significant afterglow properties, so triplet-to-triplet excited state energy transfer is not necessary for the emergency of afterglow properties in the present study. In the present study, although the IBF_2-PhB-0.05% samples possess a relatively large ΔE_{ST} of 0.54 eV (S_1 level, 2.95 eV; T_1 level, 2.41 eV), the heavy atom effect of the iodine substituents can enhance intersystem crossing for the population of the triplet excited states in IBF_2-PhB-0.05% samples. The afterglow properties of IBF_2-PhB-0.05% samples can be exclusively attributed to the phosphorescence decay of molecularly dispersed IBF_2 triplet excited states in PhB matrices.

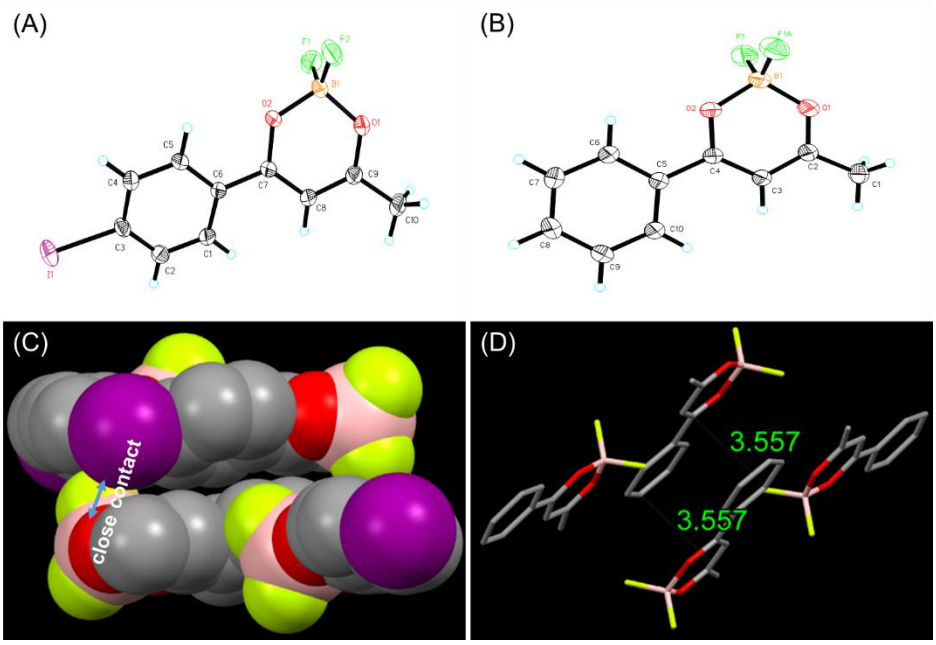

Figure S21. (A, C) Single-crystal structures of IBF_2. Due to their relatively large sizes, the iodine atoms have close contact with the dioxaborine rings of the neighbouring IBF_2 molecules (C), which leads to the formation of external heavy atom effect in IBF_2 powders, as well as IBF_2-PhB powders at high doping concentrations. (B, D) Single-crystal structures of HBF_2. It is found that the HBF_2 molecules show π–π stacking with an interplanar distance of 0.356 nm.

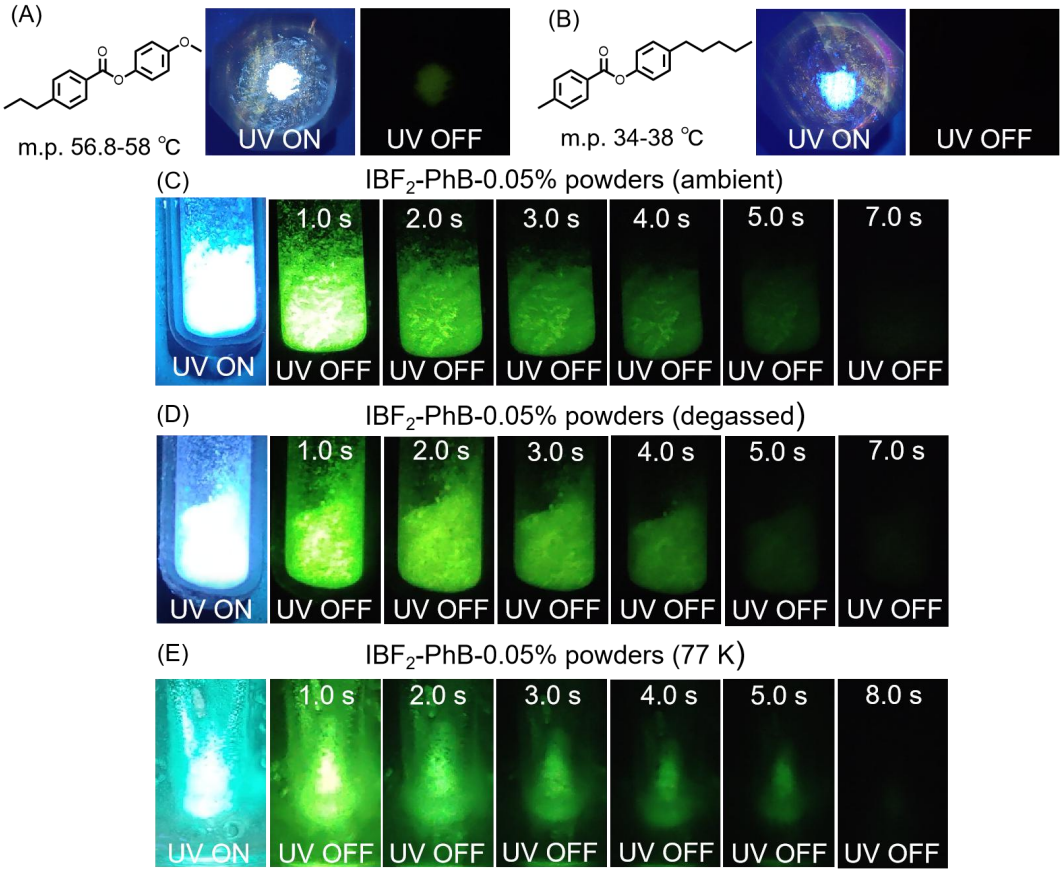

Figure S22. (A) Chemical structure of 4-methoxyphenyl 4-propylbenzoate and photographs of the IBF_2-4-methoxyphenyl 4-propylbenzoate-0.05% samples under 365 nm UV light and after removal of 365 nm UV light. (B) Chemical structure of 4-pentylphenyl 4-methylbenzoate and IBF_2-4-methoxyphenyl 4-propylbenzoate-0.05% samples under 365 nm UV light and after removal of 365 nm UV light. (C-E) Photographs of IBF_2-PhB-0.05% powders at ambient conditions (C), in degassed conditions (D) and at 77 K (E) under 365 nm UV light and after removal of 365 nm UV light. PhB derivatives such as 4-methoxyphenyl 4-propylbenzoate and 4-pentylphenyl 4-methylbenzoate have been tested as organic matrix for the preparation of IBF_2-matrix samples. These IBF_2-matrix samples show insignificant afterglow at ambient conditions. When compared to PhB matrices, these PhB derivatives possess lower melting points and can only provide microenvironments with less rigidity. It is also found that the afterglow durations of the IBF_2-PhB-0.05% materials at 77 K where nonradiative decay is frozen are only slightly longer than those at ambient conditions. These experiments suggest that the rigid microenvironments provided by PhB organic matrices can restrict the nonradiative deactivation of IBF_2 triplet excited states at ambient conditions. The afterglow properties of the IBF_2-PhB-0.05% materials in degassed conditions have also been tested. It has also been found that the IBF_2-PhB-0.05% materials in degassed conditions possess similar afterglow brightness and duration as the materials at ambient conditions. These suggest that the PhB can protect the IBF_2 triplet excited states from oxygen quenching by the encapsulation. For the IBF_2-PhB-0.05% materials at ambient conditions, the rate constant of phosphorescence decay (k_P) can be estimated from their phosphorescence lifetimes to be on the order of 1 s^{-1}. The k_{nr} values are dependent on the environments of IBF_2 triplet excited states. At 77 K, the k_{nr} is much smaller than k_P since the molecular motion at low temperature can be largely suppressed. It is found that the afterglow durations of the IBF_2-PhB-0.05% materials at 77 K are slightly longer than those at ambient condition. These suggest that the k_{nr} is much smaller than k_P because the rigid PhB matrices can largely restrict intramolecular motions of the IBF_2 triplet excited states even at room temperature. The insignificant difference of the afterglow durations between ambient conditions and degassed conditions suggest that the k_q with oxygen of the IBF_2-PhB-0.05% materials should be smaller than k_P because of the PhB encapsulation. Without the presence of PhB matrices, the IBF_2-matrix-0.05% samples (when 4-methoxyphenyl 4-propylbenzoate and 4-pentylphenyl 4-methylbenzoate are used as matrix) show insignificant afterglow, which suggest that the $k_{nr} + k_q$ values are larger than k_P in these systems.

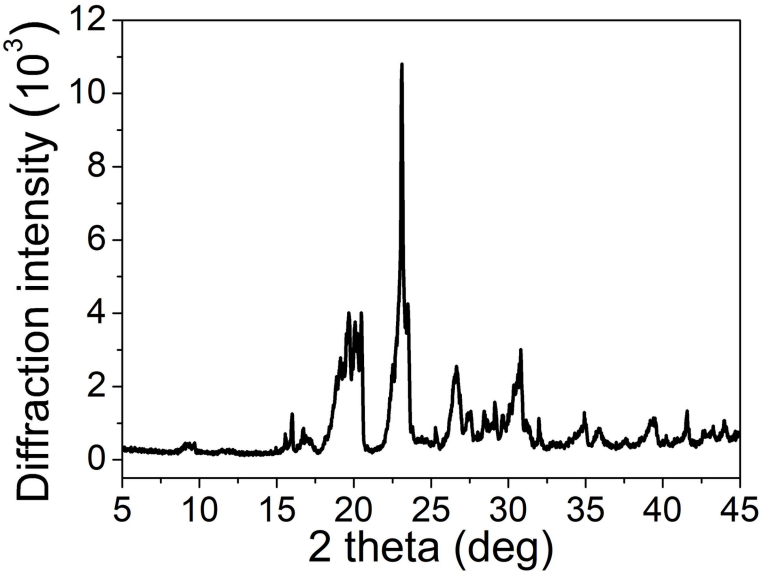

Figure S23. Powder XRD pattern of the melt-cast film of phenyl benzoate. Powder XRD shows crystalline structures of PhB, which indicate that the PhB matrices can provide rigid microenvironments for IBF_2 triplet excited states.

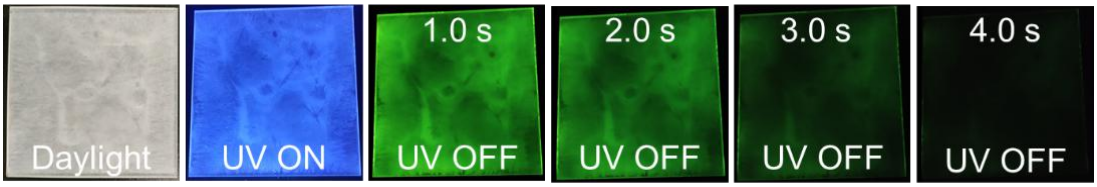

Figure S24. Photographs of IBF_2-PhB-0.05% afterglow film sandwiched between two 10 cm × 10 cm quartz plates under daylight, 365 nm UV light and after removal of 365 nm UV light.

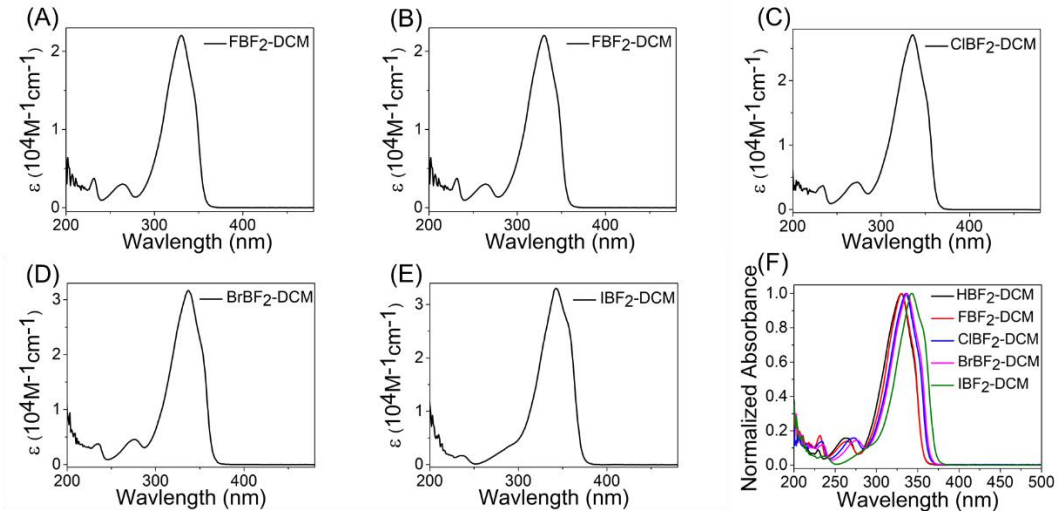

Figure S25. UV-Vis spectra of the BF_2bdk compounds in dichloromethane solutions in the present study.

Table S1. Photophysical data of HBF_2, FBF_2, $ClBF_2$, $BrBF_2$ and IBF_2 at room temperature.

Entry	HBF_2 (DCM)	FBF_2 (DCM)	$ClBF_2$ (DCM)	$BrBF_2$ (DCM)	IBF_2 (DCM)
λ_{Abs} (nm)	330	330	336	337	343
ε ($10^4 M^{-1}cm^{-1}$)	2.51	2.20	2.71	3.17	3.30

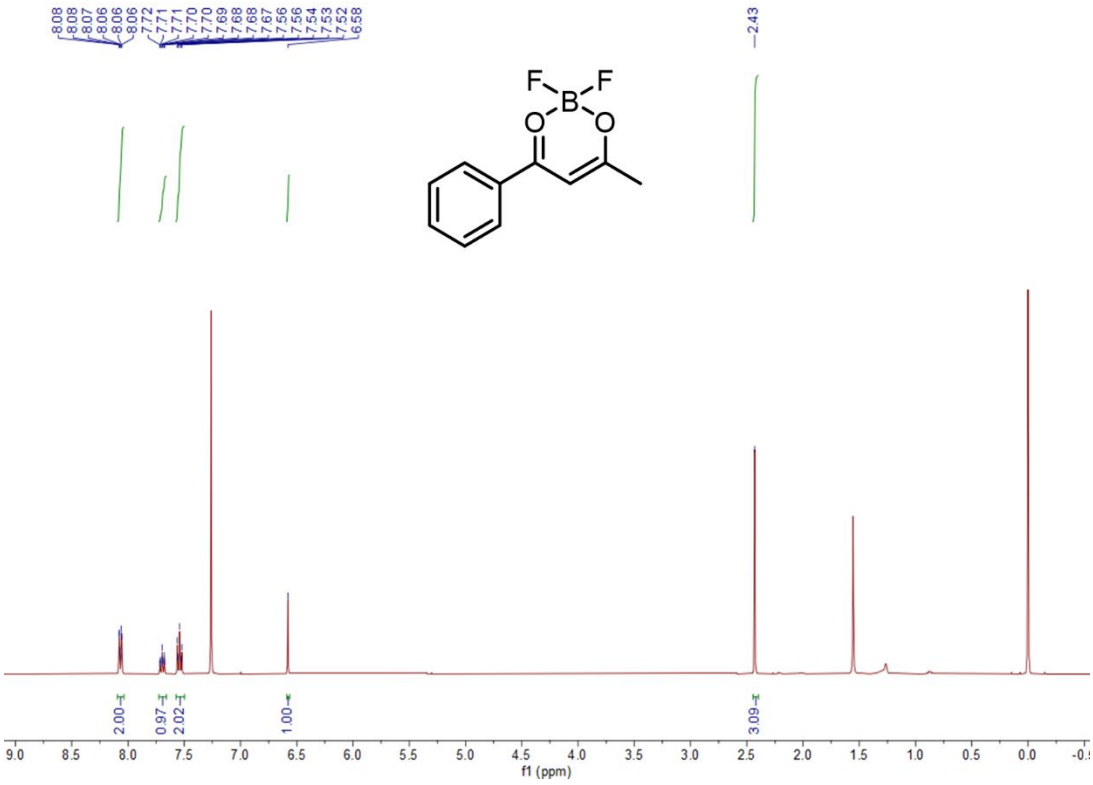

Figure S26. ^{1}H NMR spectrum of HBF_2.

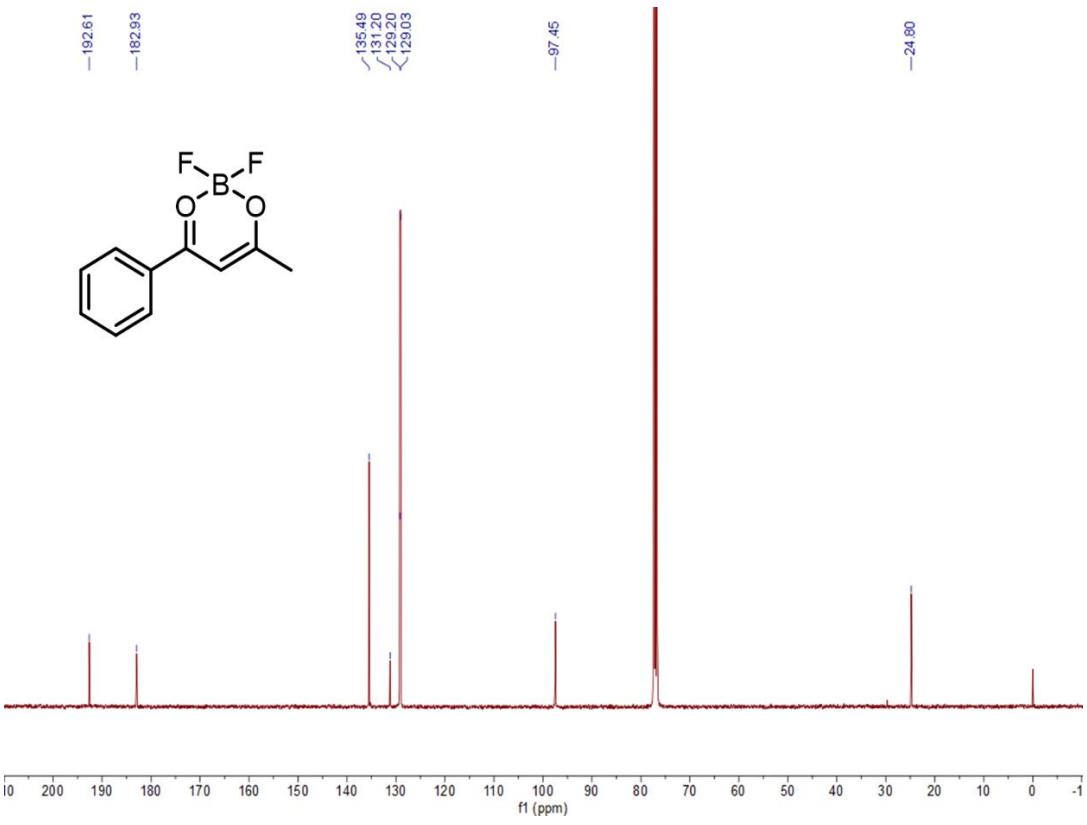

Figure S27. ^{13}C NMR spectrum of HBF_2.

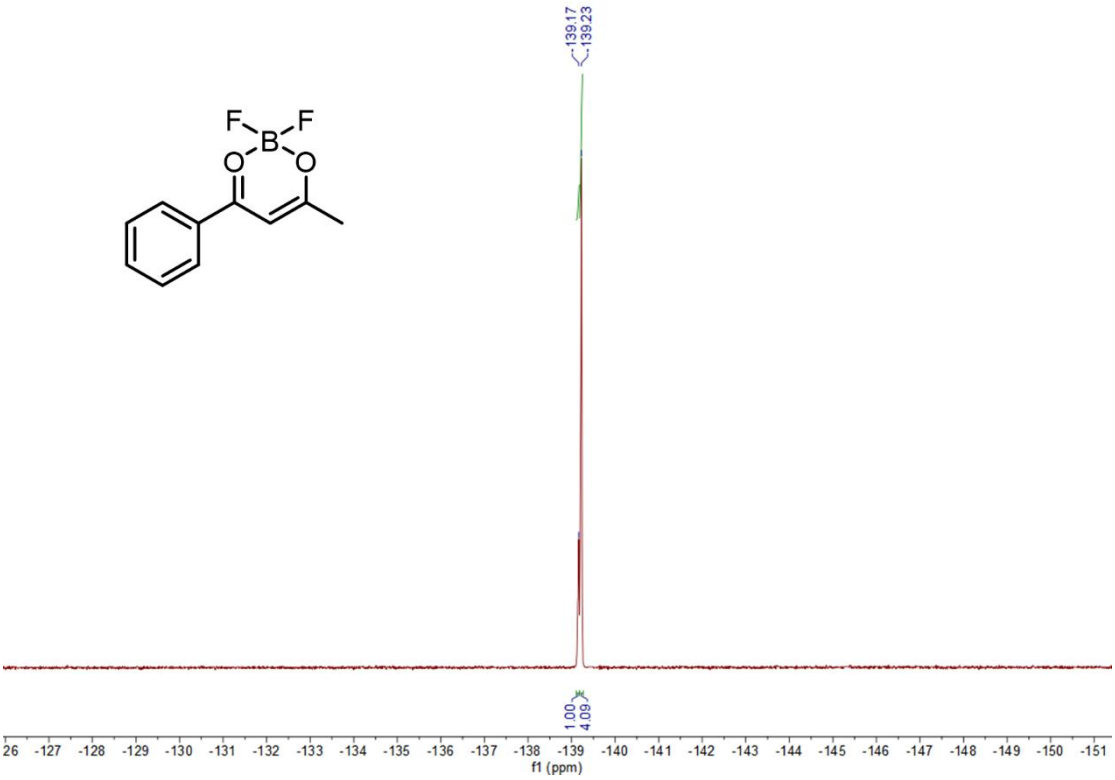

Figure S28. ^{19}F NMR spectrum of HBF_2 .

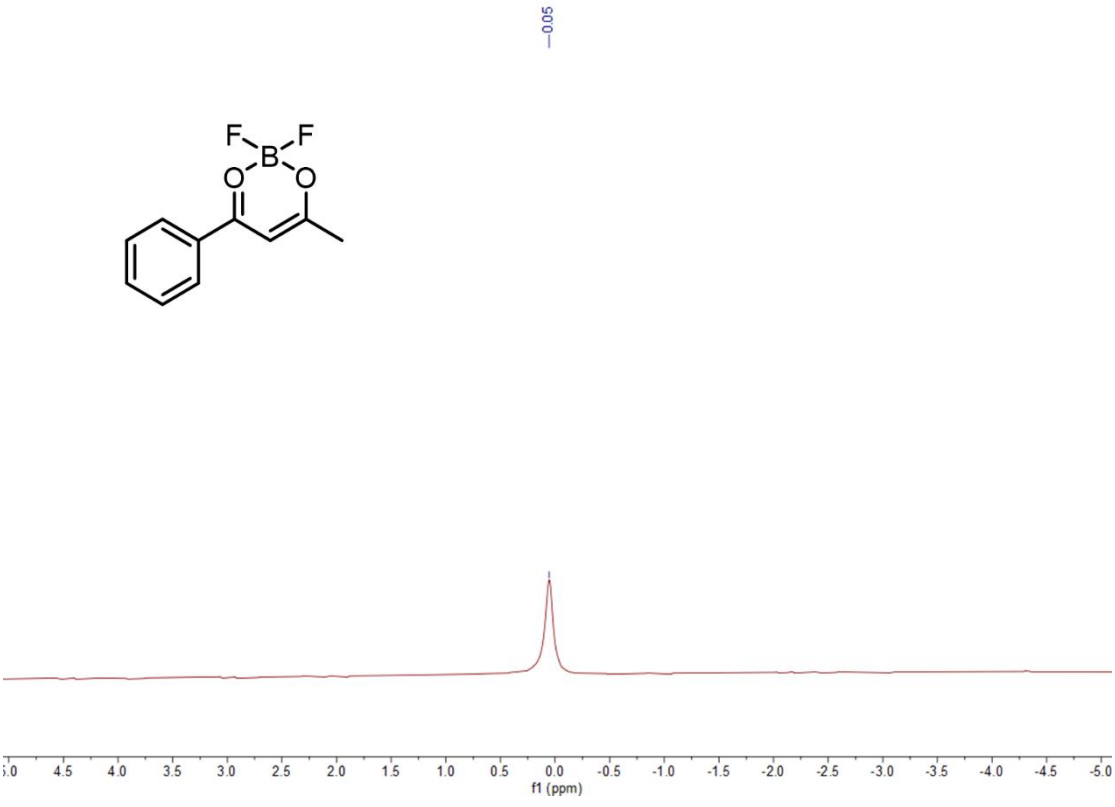

Figure S29. ^{11}B NMR spectrum of HBF_2.

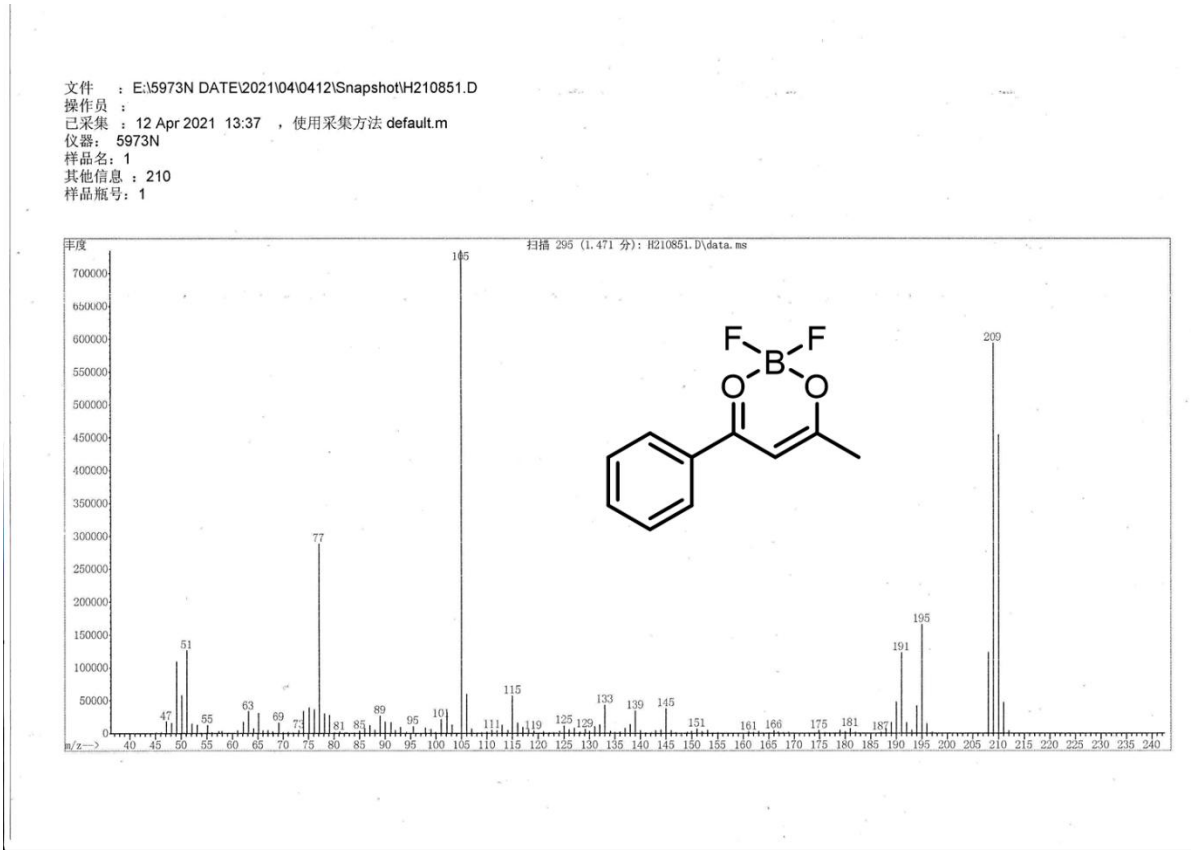

Figure S30. LRMS spectrum of HBF_2.

National Center for Organic Mass Spectrometry in Shanghai
Shanghai Institute of Organic Chemistry
Chinese Academic of Sciences
High Resolution FI-MS Report
Low Resolution FI-MS Report

Instrument: JEOL-AccuTOF-GCv4G-GCT MS

Operation Mode: FI Positive Ion Mode (Counter Electrode: 10000V)

Card Serial Number: GCT-FI-T21-04-1487

Sample Serial Number: 2020274-1

Operator: Li Date: 2021/04/18

m/z	Theo. Mass	Delta (ppm)	RDB equiv.	Composition
209.0690	209.0694	-2.15	6.0	$C_{10}H_9O_2{}^{10}BF_2$
	209.0696	-3.05	3.5	$C_8H_9N_2F_4$
	209.0683	3.32	10.0	$C_{13}H_8O{}^{10}BF$
	209.0683	3.54	6.0	$C_{10}H_{11}O_4N$
	209.0681	4.30	-5.0	$C_2H_{12}O_4NF_5$

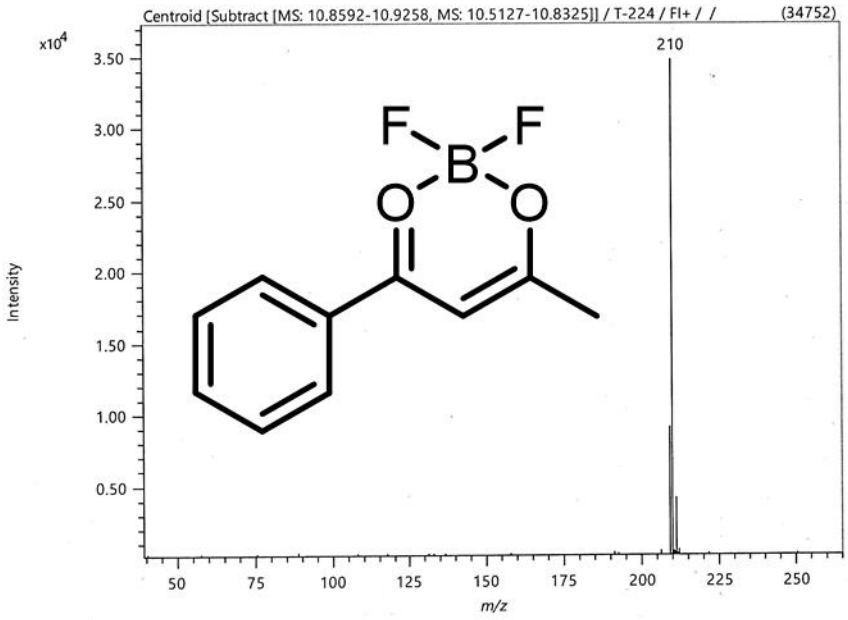

Figure S31. HRMS spectrum of HBF_2.

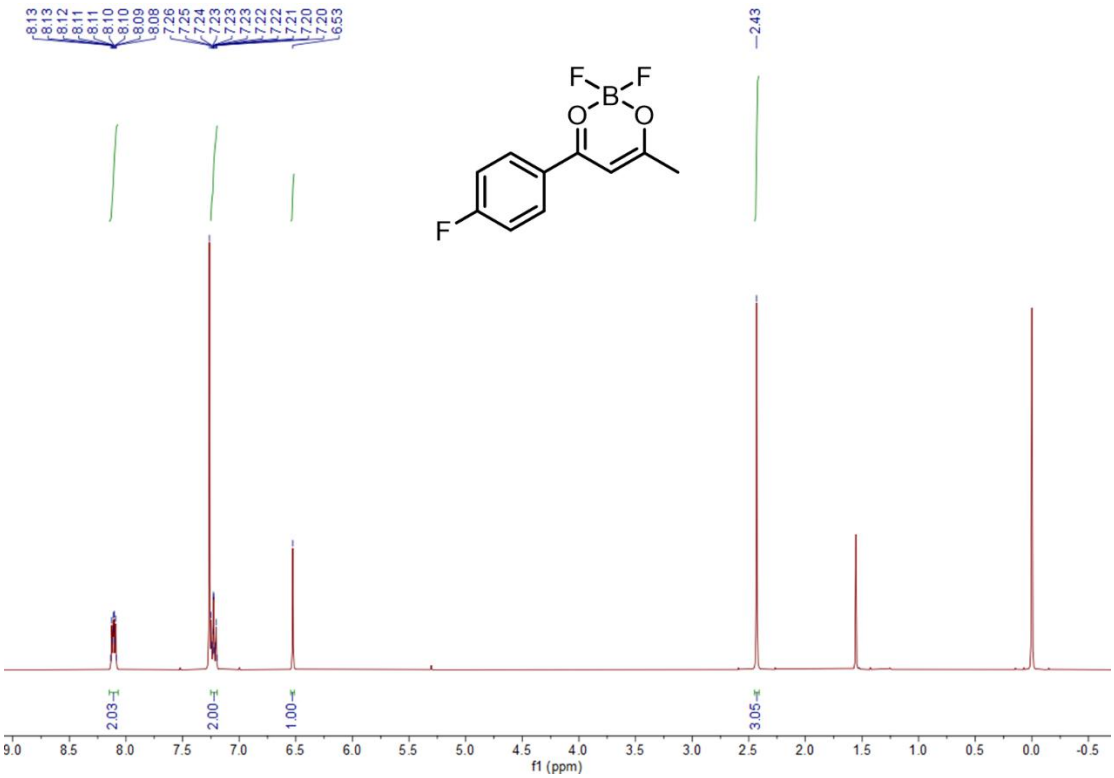

Figure S32. ^{1}H NMR spectrum of FBF_2

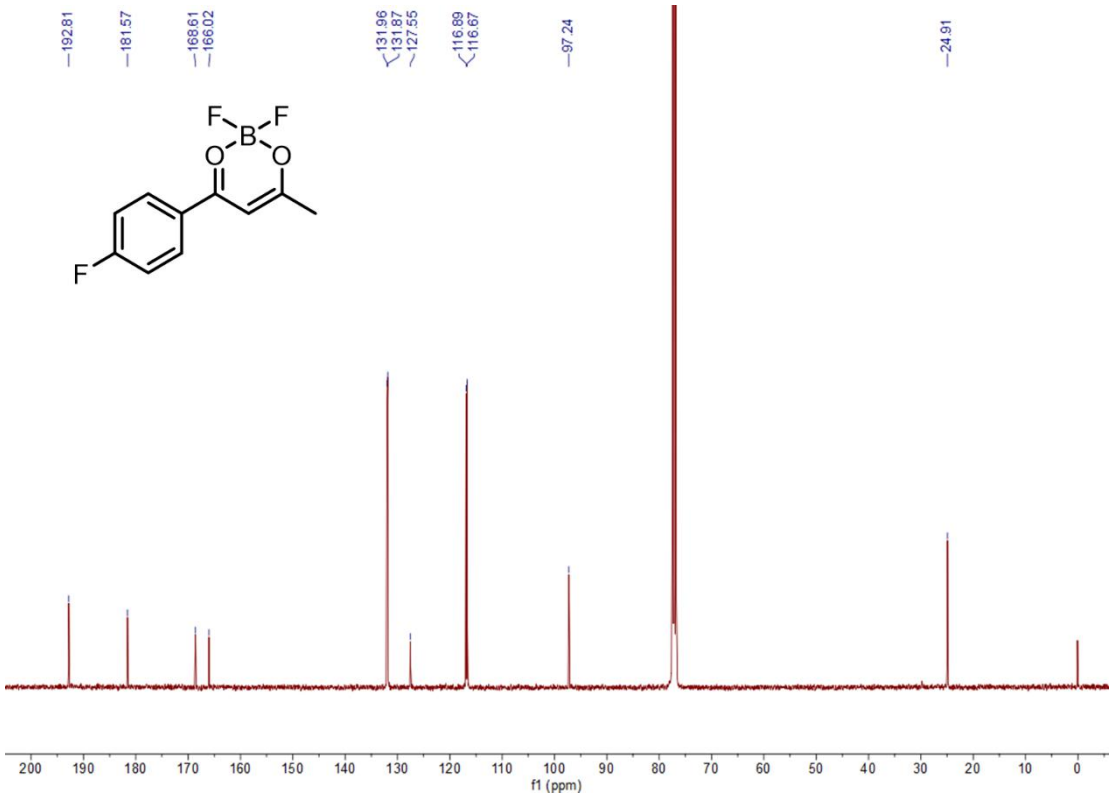

Figure S33. ^{13}C NMR spectrum of FBF_2

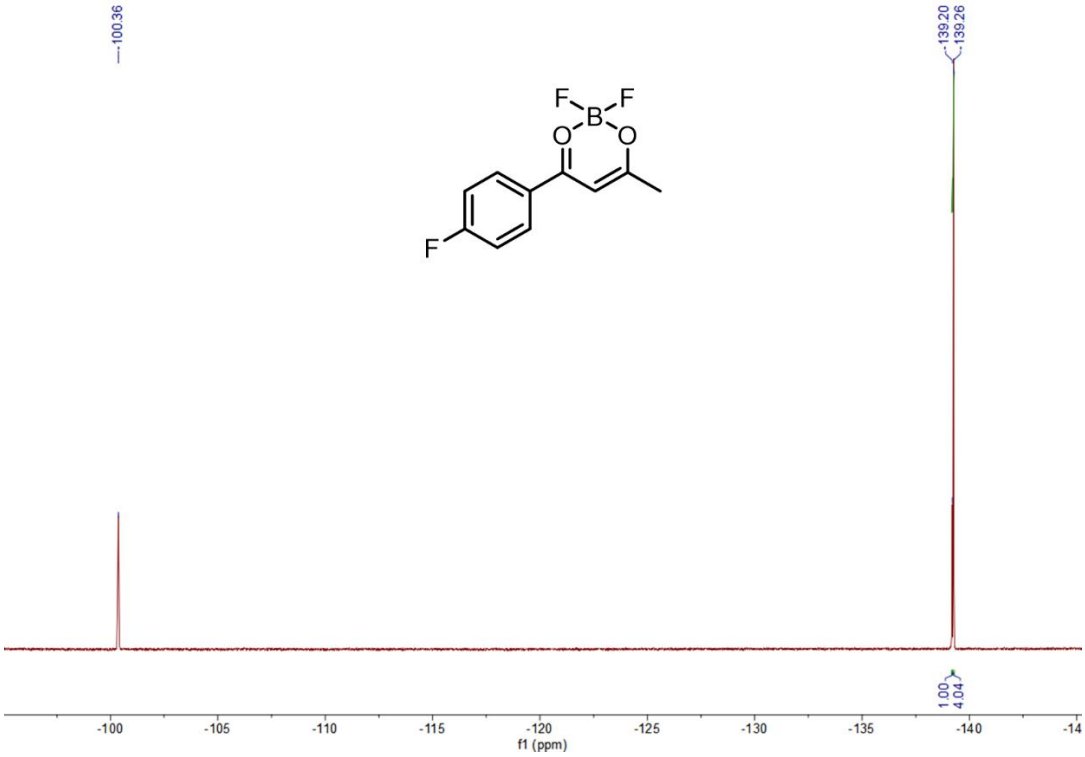

Figure S34. ^{19}F NMR spectrum of FBF_2

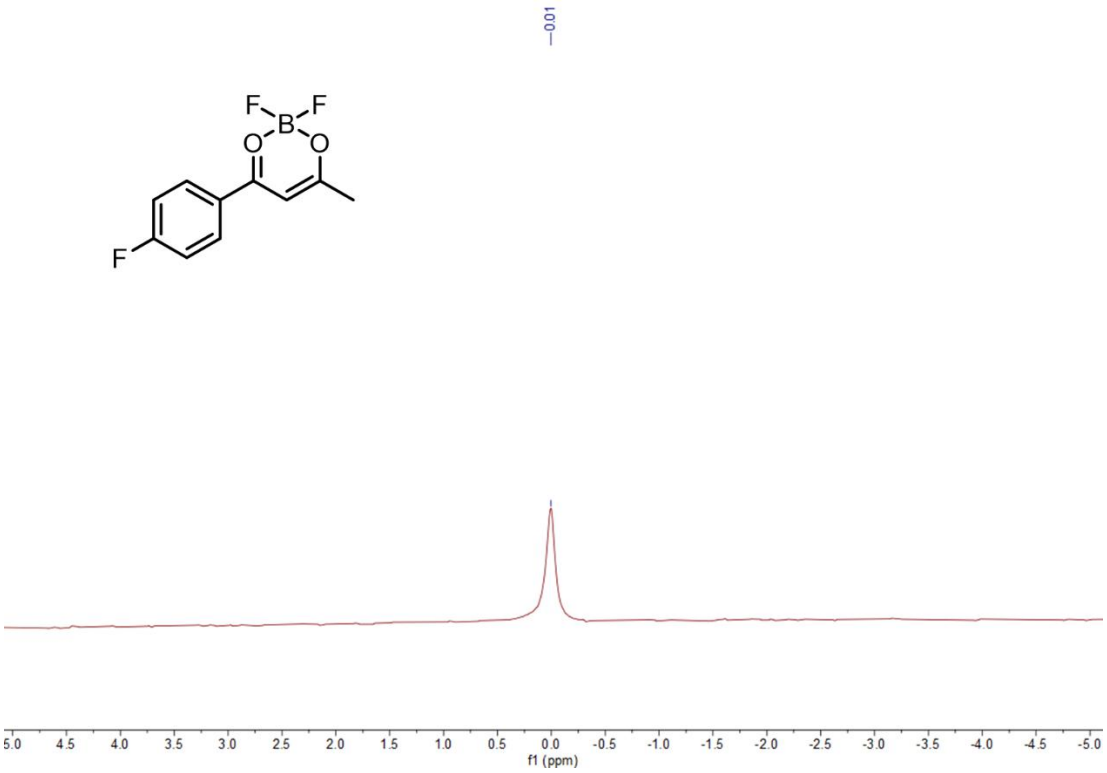

Figure S35. ^{11}B NMR spectrum of FBF_2

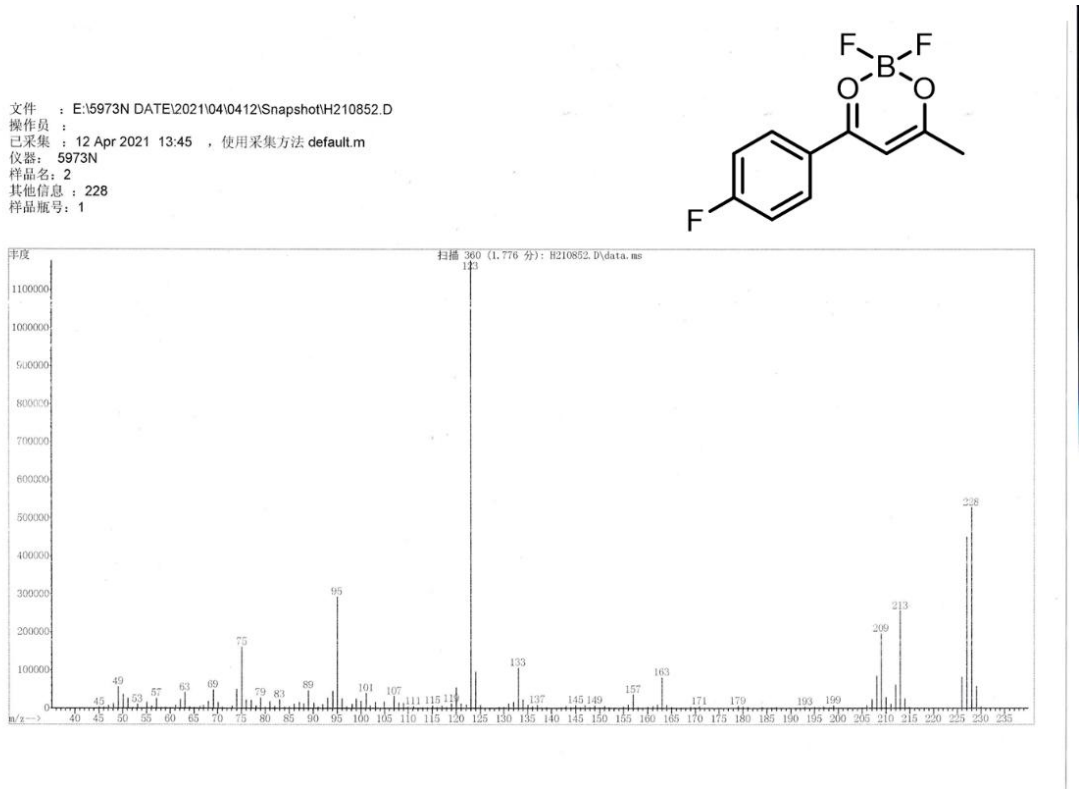

Figure S36. LRMS spectrum of FBF_2.

National Center for Organic Mass Spectrometry in Shanghai
Shanghai Institute of Organic Chemistry
Chinese Academic of Sciences
High Resolution FI-MS Report
Low Resolution FI-MS Report

Instrument: JEOL-AccuTOF-GCv4G-GCT MS

Operation Mode: FI Positive Ion Mode (Counter Electrode: 10000V)

Card Serial Number: GCT-FI-T21-04-1488

Sample Serial Number: 2020274-2

Operator: Li Date: 2021/04/18

m/z	Theo. Mass	Delta (ppm)	RDB equiv.	Composition
227.0597	227.0600	-1.44	6.0	$C_{10}H_8O_2{}^{10}BF_3$
	227.0602	-2.27	3.5	$C_8H_8N_2F_5$
	227.0604	-2.97	14.5	$C_{16}H_7N_2$
	227.0589	3.59	10.0	$C_{13}H_7O{}^{10}BF_2$
	227.0588	3.80	6.0	$C_{10}H_{10}O_4NF$

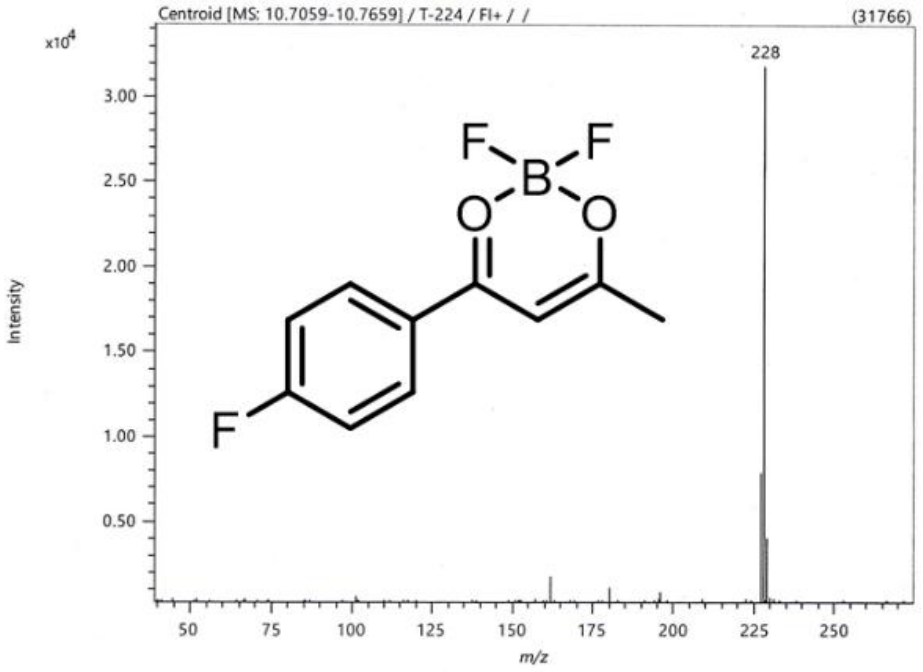

Figure S37. HRMS spectrum of FBF_2

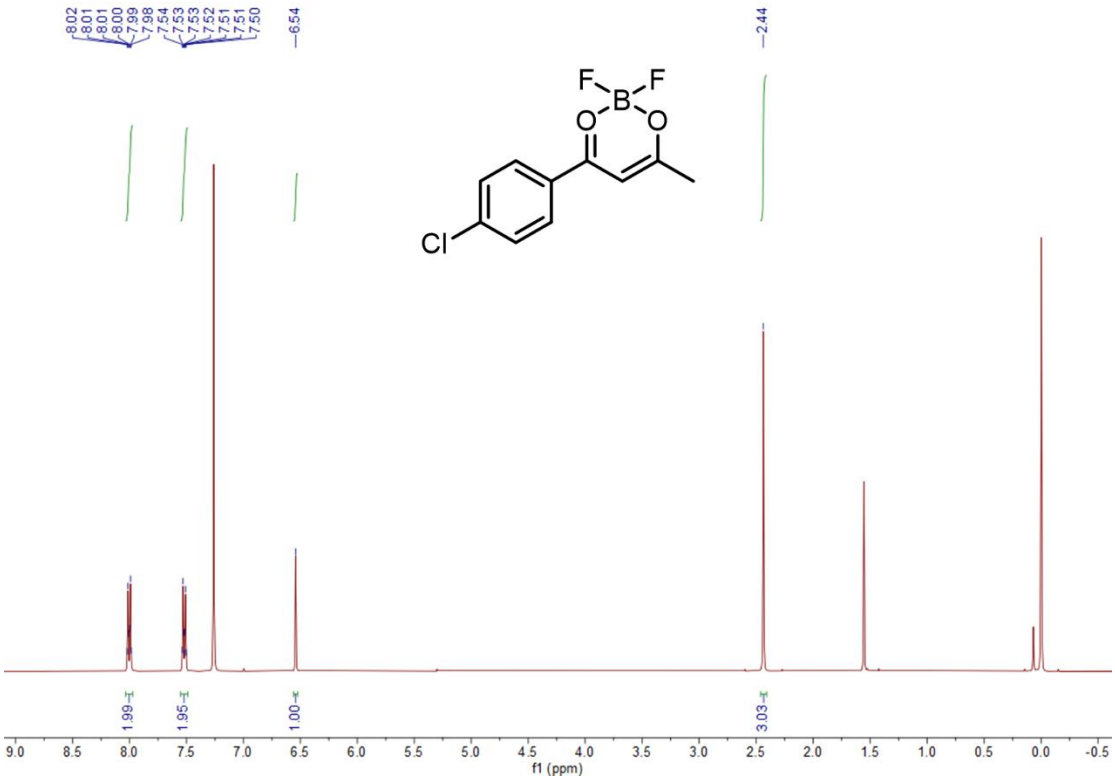

Figure S38. ^{1}H NMR spectrum of $ClBF_2$

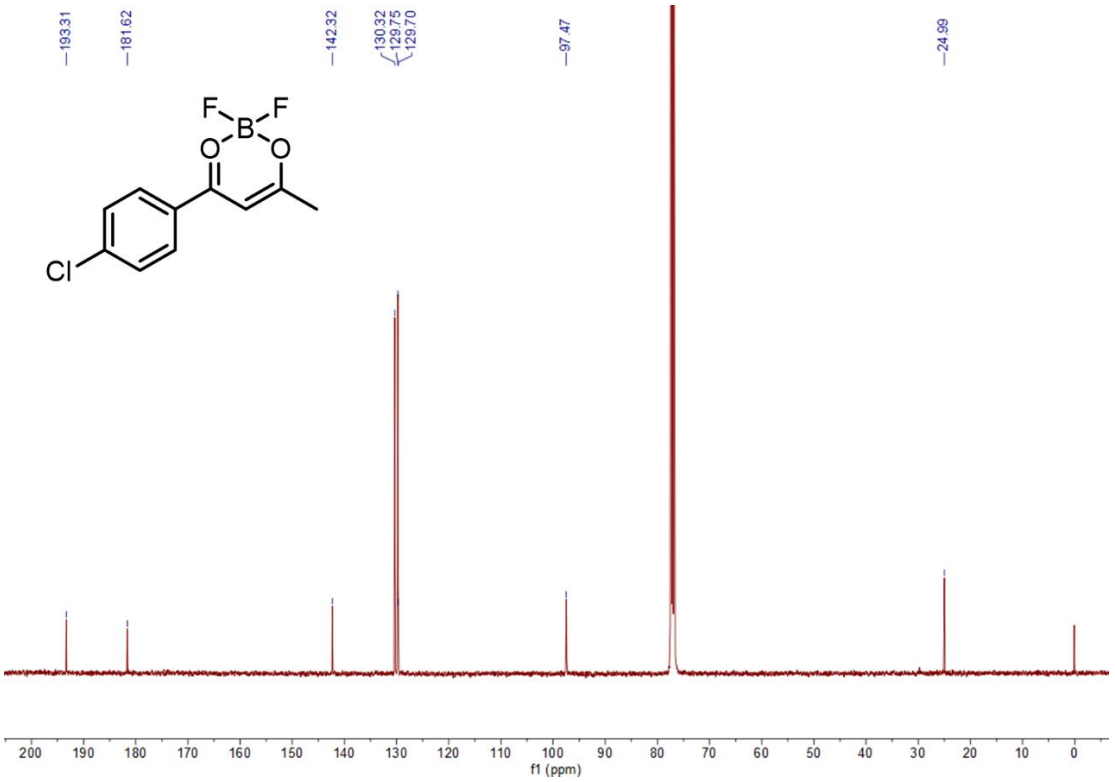

Figure S39. ^{13}C NMR spectrum of $ClBF_2$

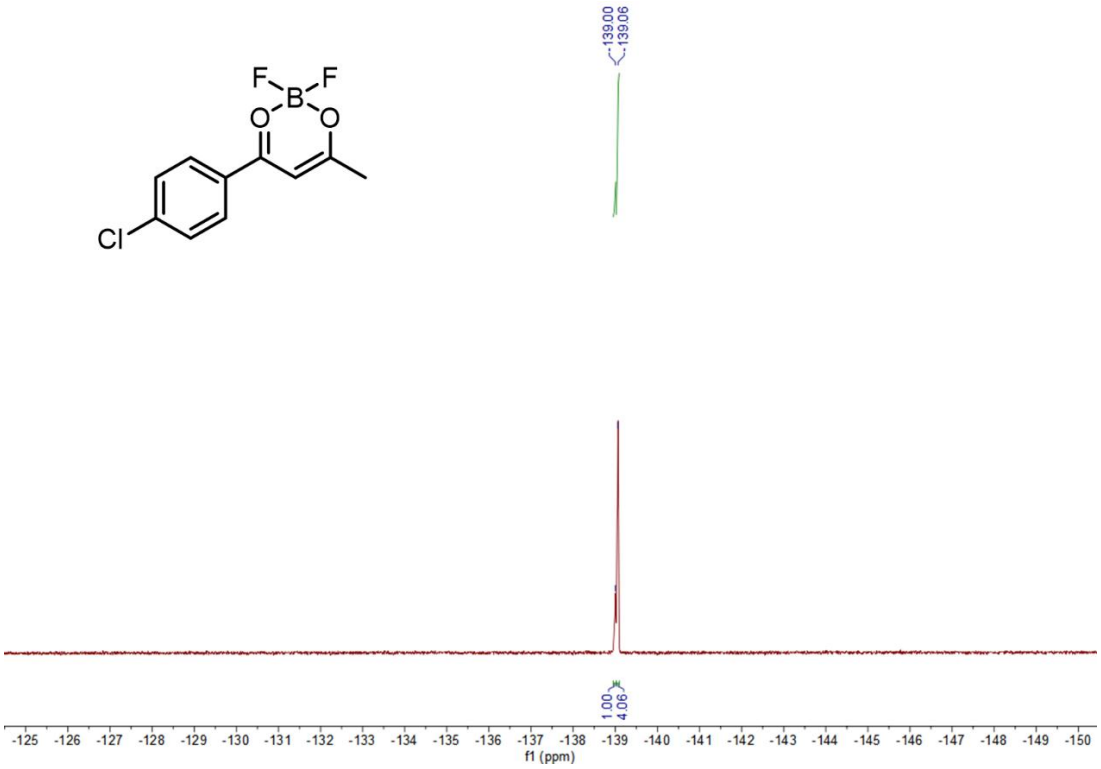

Figure S40. ^{19}F NMR spectrum of $ClBF_2$

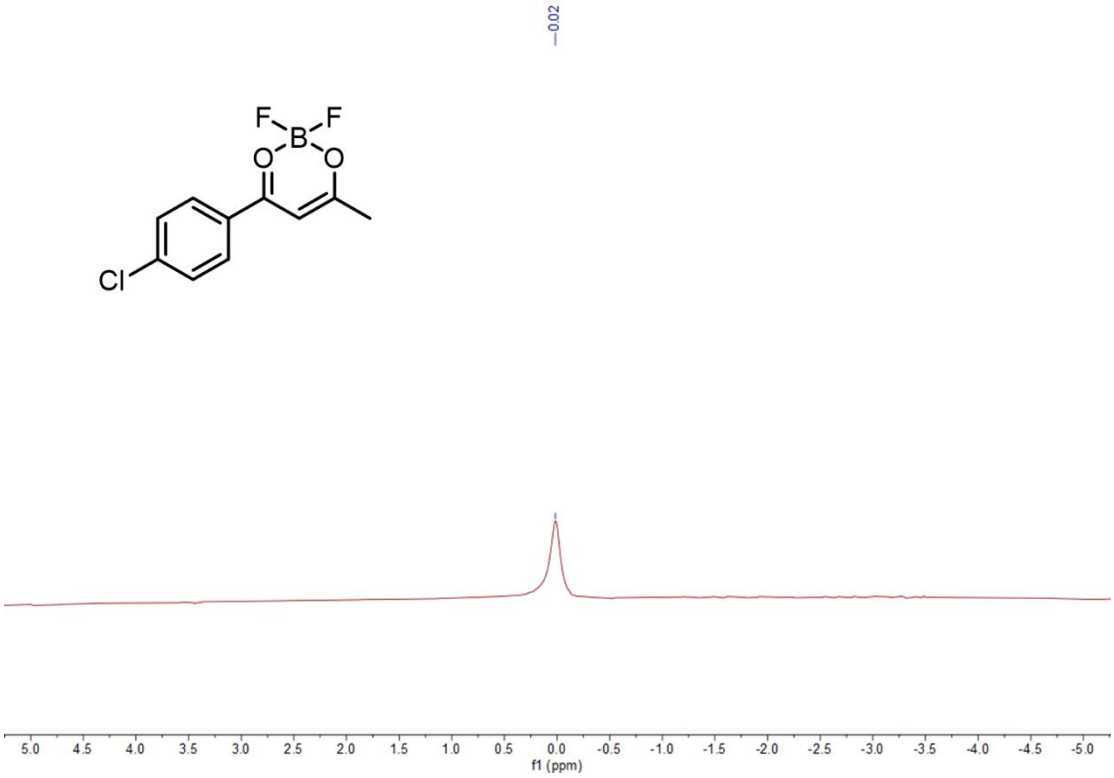

Figure S41. ^{11}B NMR spectrum of $ClBF_2$

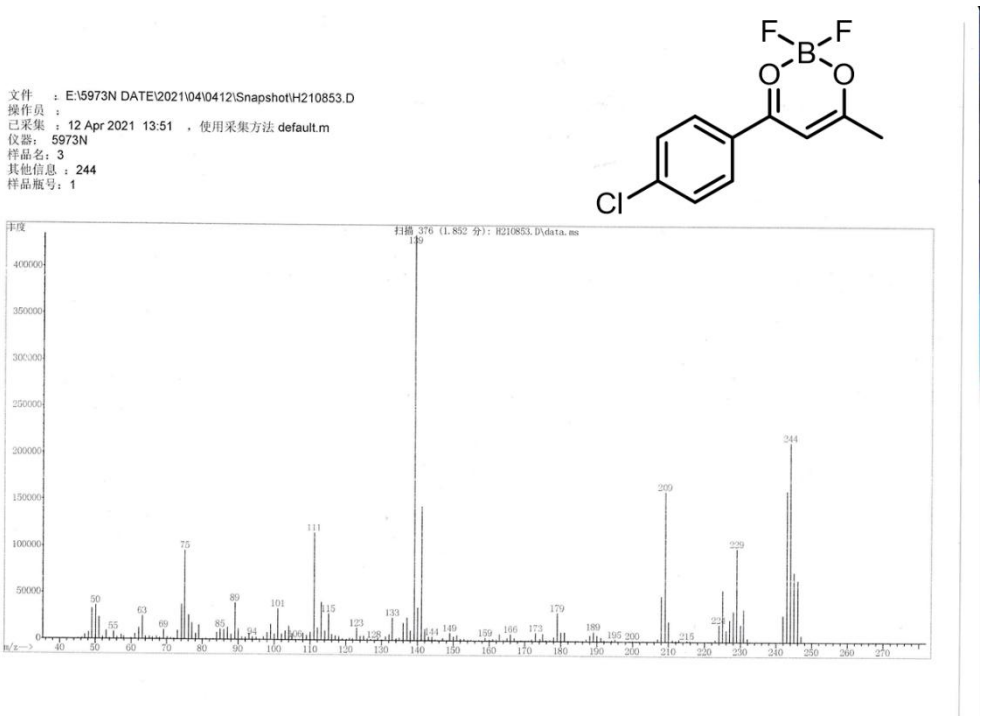

Figure S42. LRMS spectrum of $ClBF_2$.

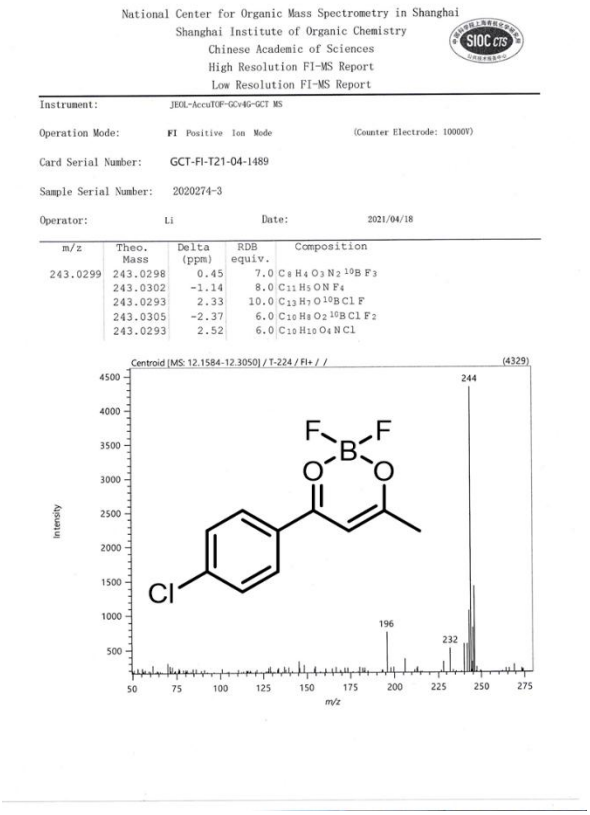

Figure S43. HRMS spectrum of $ClBF_2$.

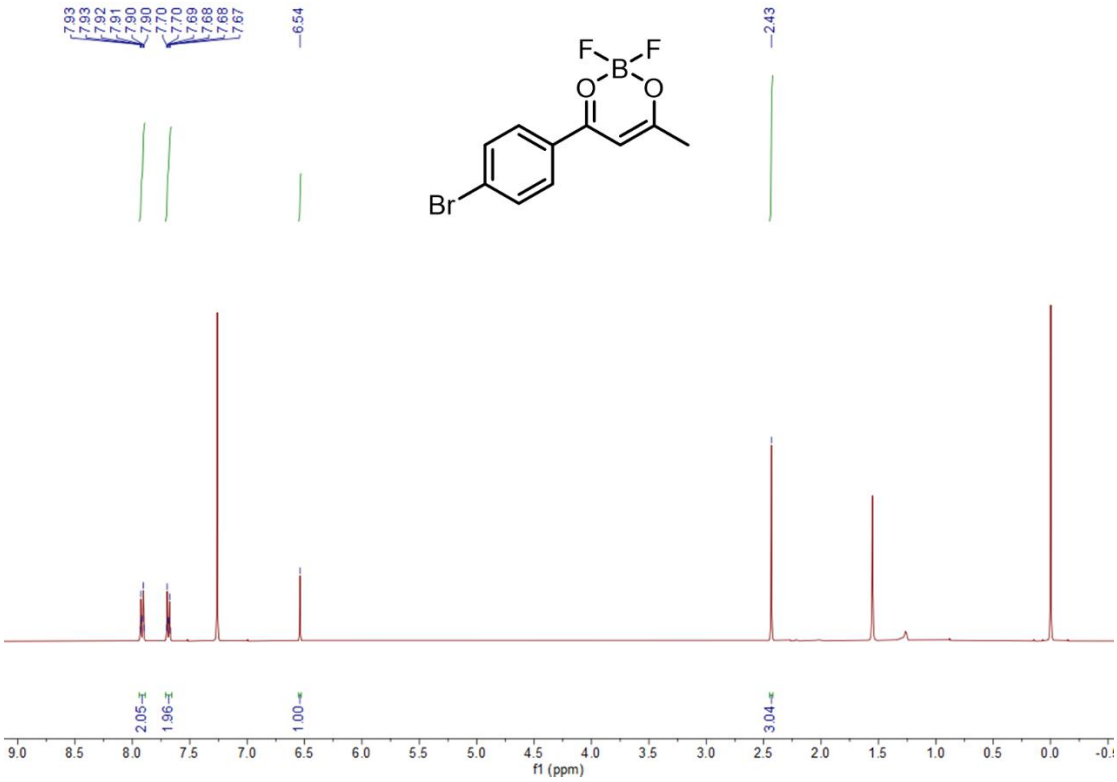

Figure S44. ^{1}H NMR spectrum of $BrBF_2$

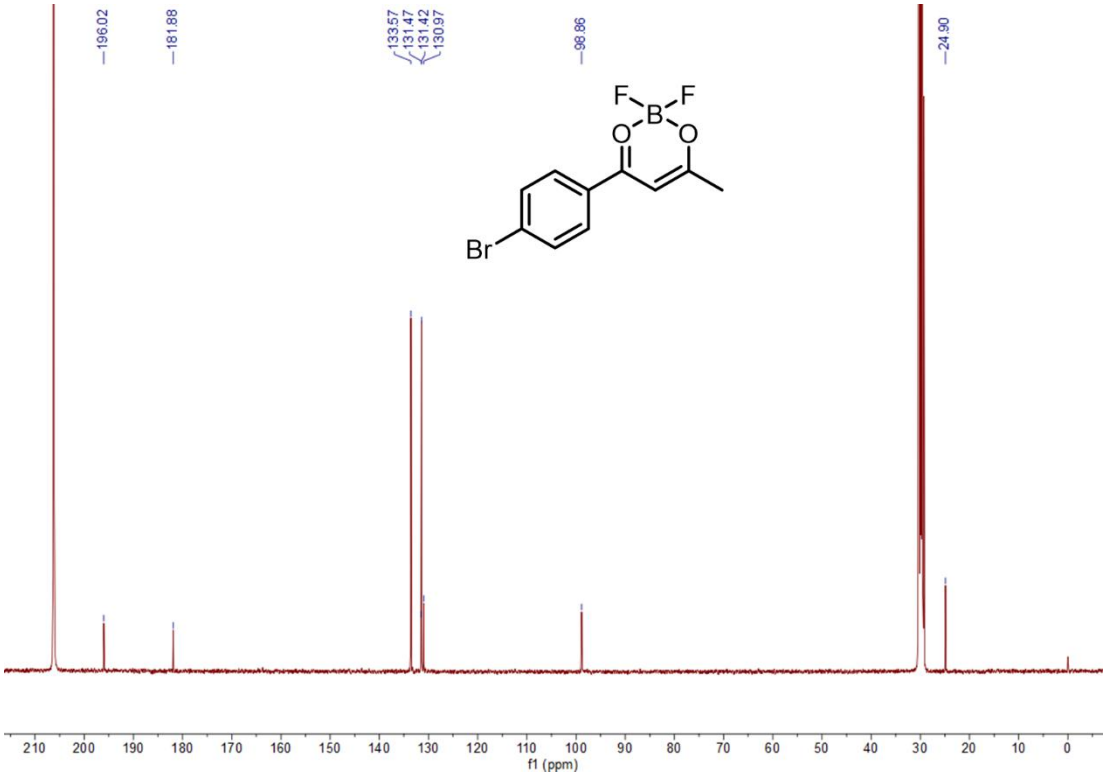

Figure S45. ^{13}C NMR spectrum of $BrBF_2$

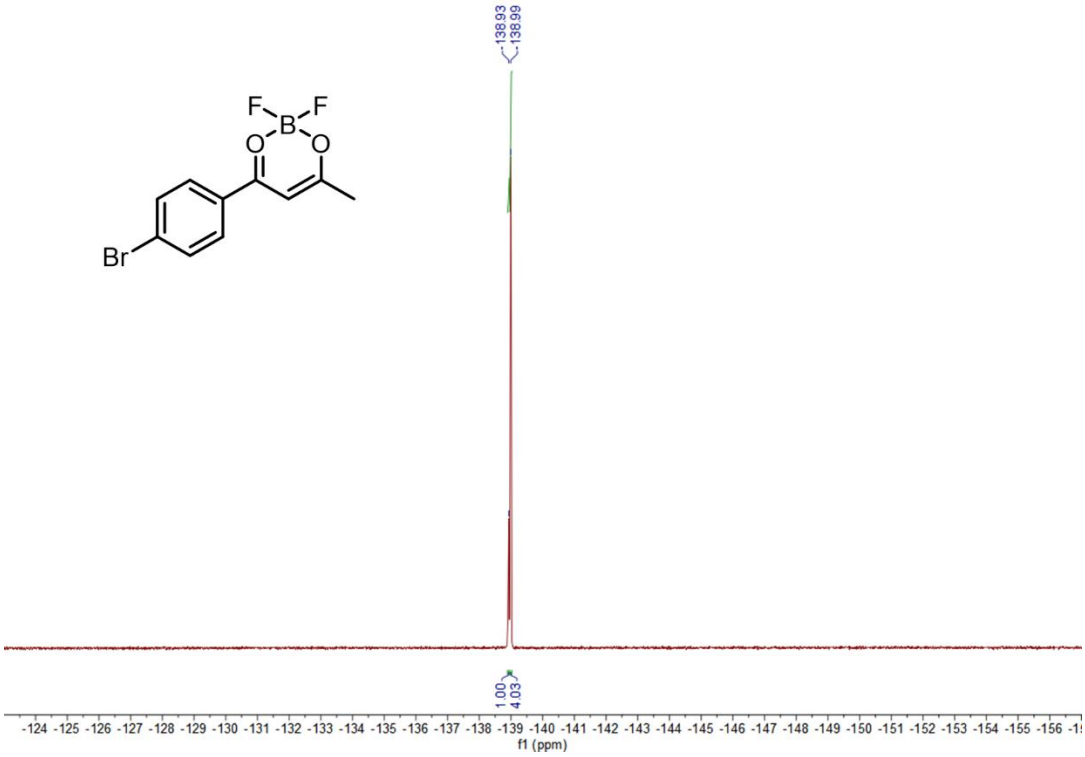

Figure S46. ^{19}F NMR spectrum of $BrBF_2$

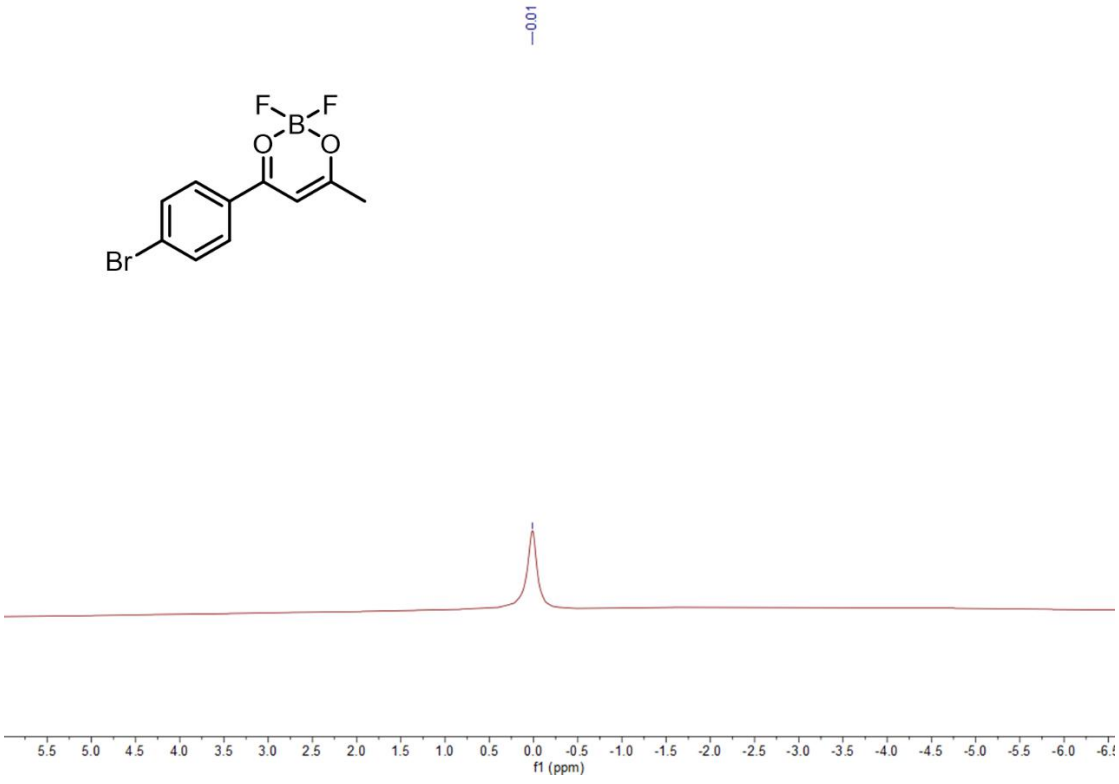

Figure S47. ^{11}B NMR spectrum of $BrBF_2$

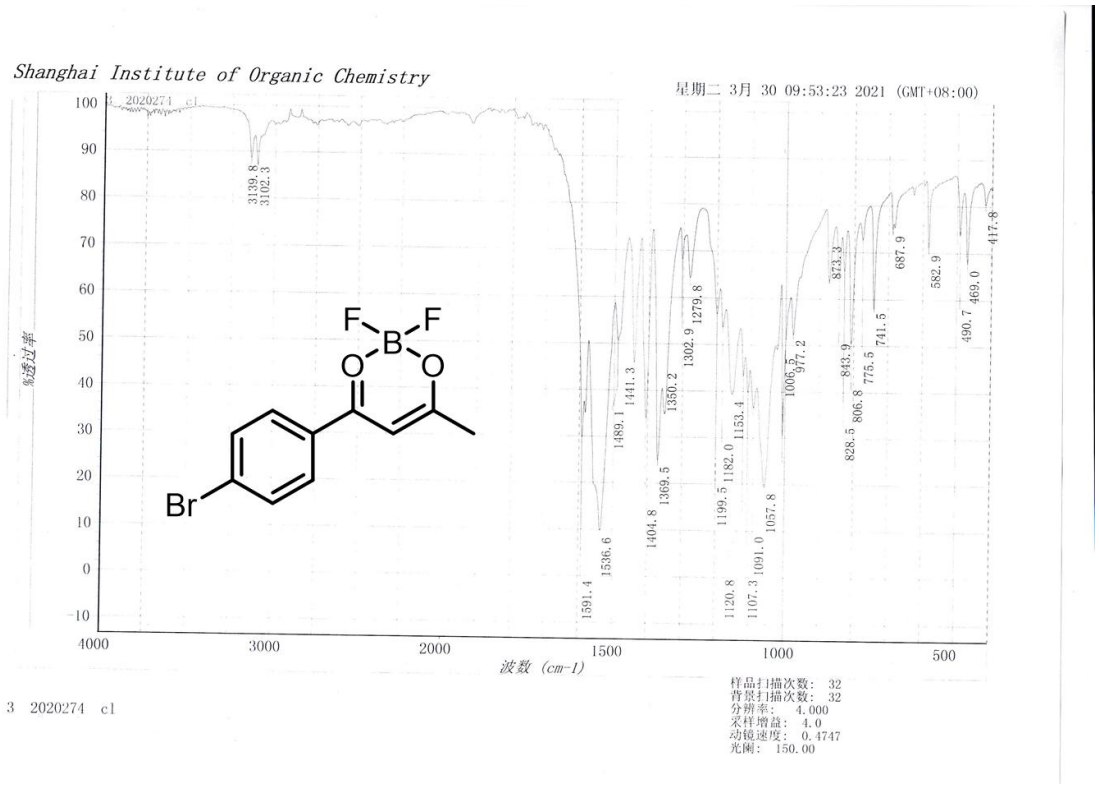

Figure S48. FT-IR spectrum of $BrBF_2$

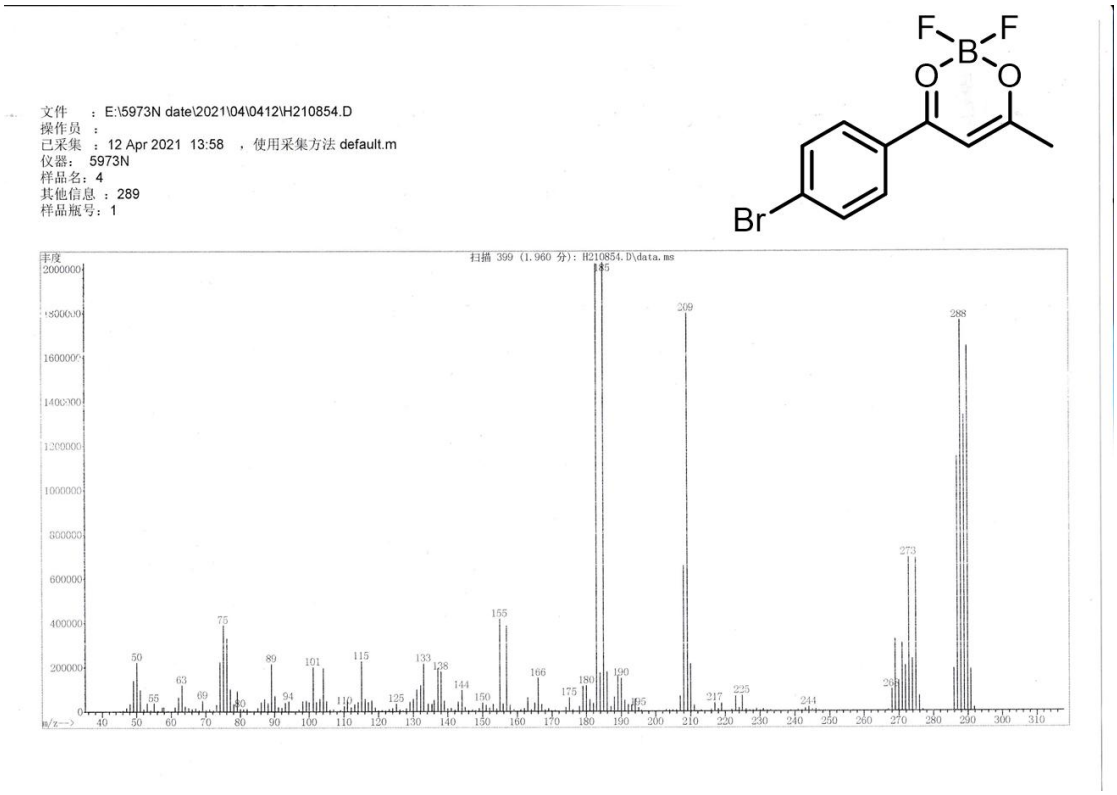

Figure S49. LRMS spectrum of $BrBF_2$

National Center for Organic Mass Spectrometry in Shanghai
Shanghai Institute of Organic Chemistry
Chinese Academic of Sciences
High Resolution FI-MS Report
Low Resolution FI-MS Report

Instrument: JEOL-AccuTOF-GCv4G-GCT MS

Operation Mode: FI Positive Ion Mode (Counter Electrode: 10000V)

Card Serial Number: GCT-FI-T21-04-1491

Sample Serial Number: 2020274-4

Operator: Li Date: 2021/04/18

m/z	Theo. Mass	Delta (ppm)	RDB equiv.	Composition
286.9795	286.9799	-1.49	-10.0	$H_{20}O_2{}^{10}B\,Br\,F\,I$
	286.9800	-1.61	6.0	$C_{10}H_8O_2{}^{10}B\,Br\,F_2$
	286.9800	-1.74	-5.0	$C_2H_{11}O\,N\,F_5\,I$
	286.9789	2.24	-1.0	$C_5H_{10}N\,F_4\,I$
	286.9802	-2.27	3.5	$C_8H_8N_2\,Br\,F_4$

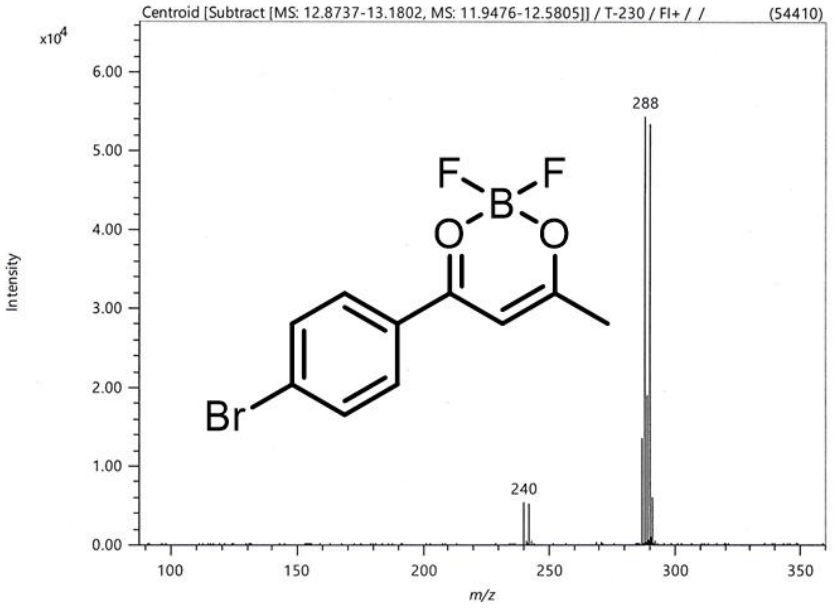

Figure S50. HRMS spectrum of $BrBF_2$

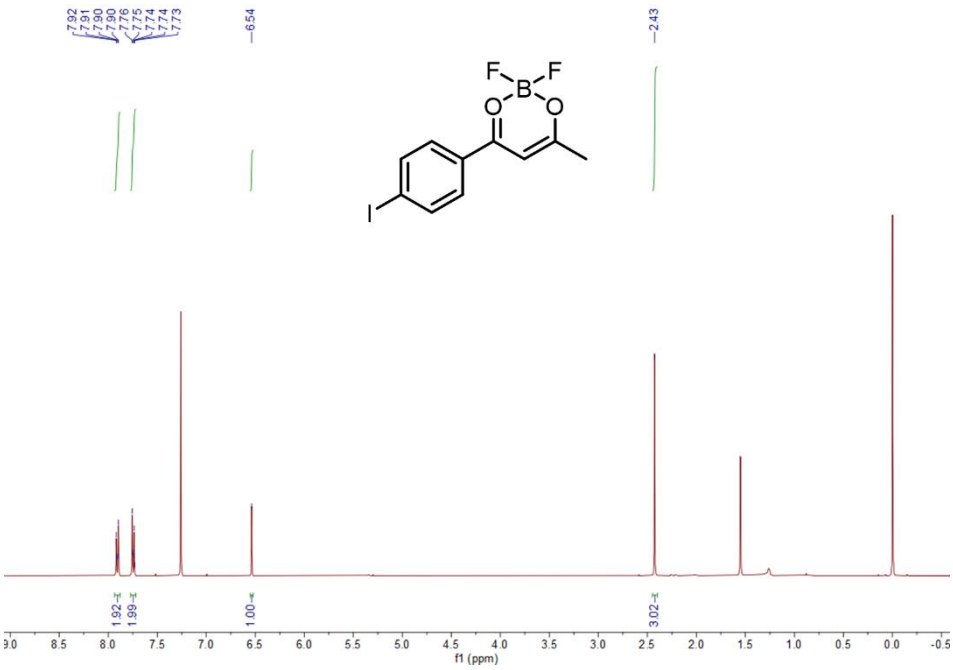

Figure S51. ^{1}H NMR spectrum of IBF_2

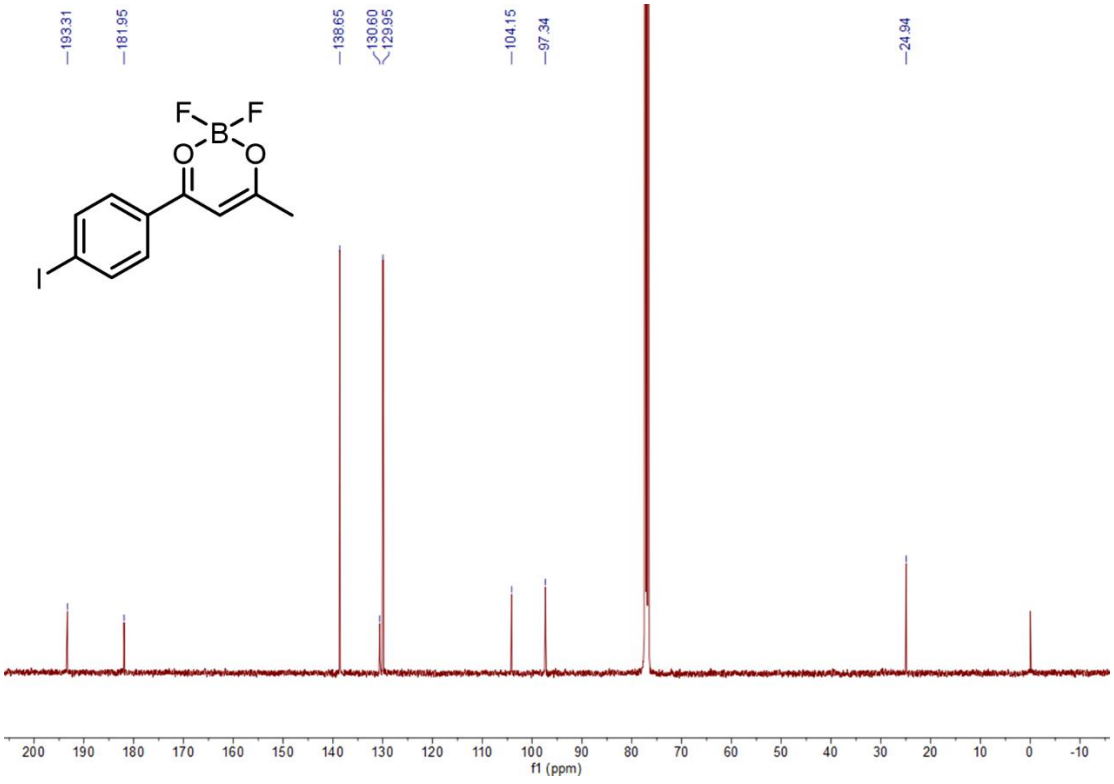

Figure S52. ^{13}C NMR spectrum of IBF_2

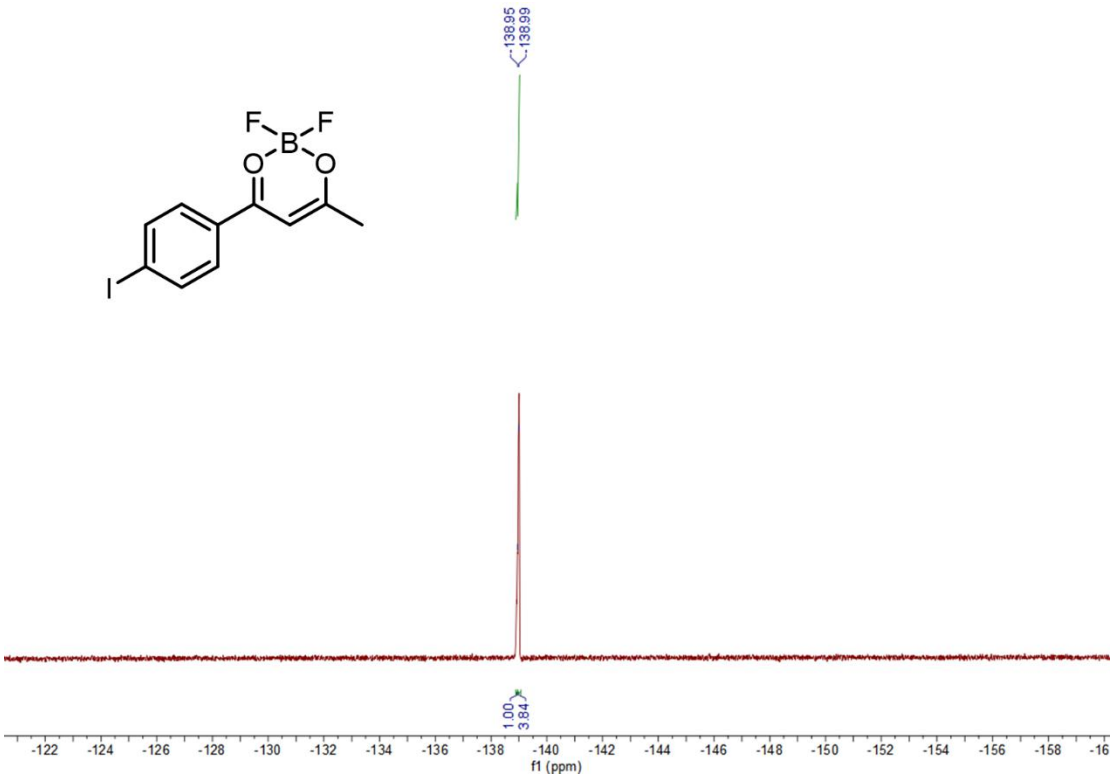

Figure S53. ^{19}F NMR spectrum of IBF_2

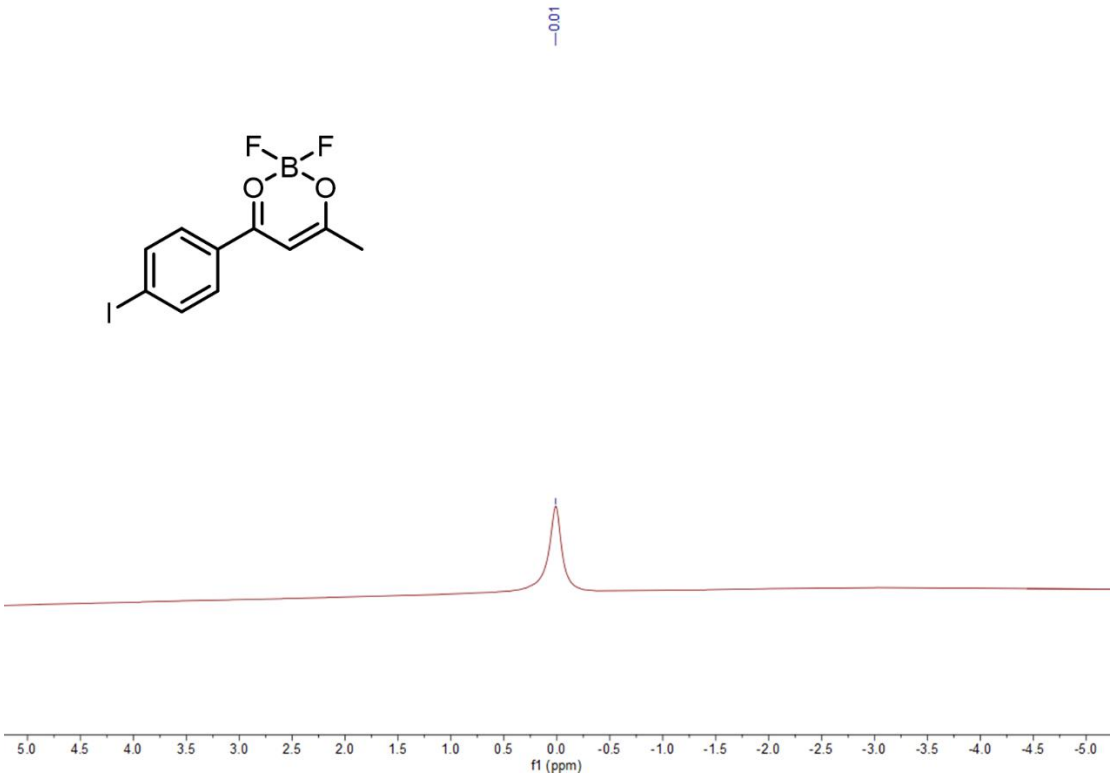

Figure S54. ^{11}B NMR spectrum of IBF_2

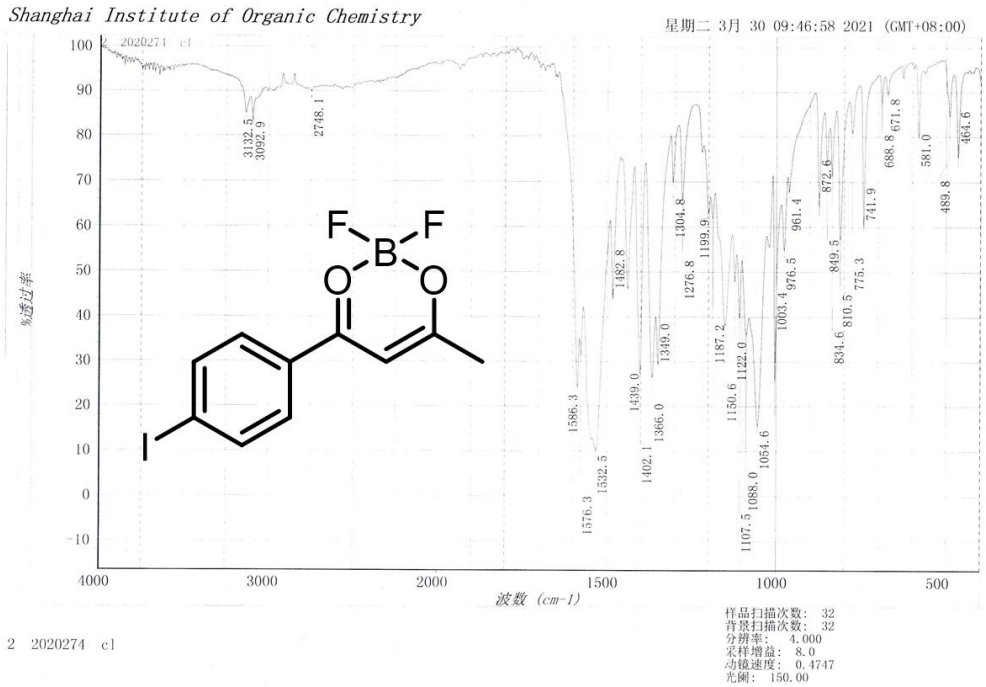

Figure S55. FT-IR spectrum of IBF_2

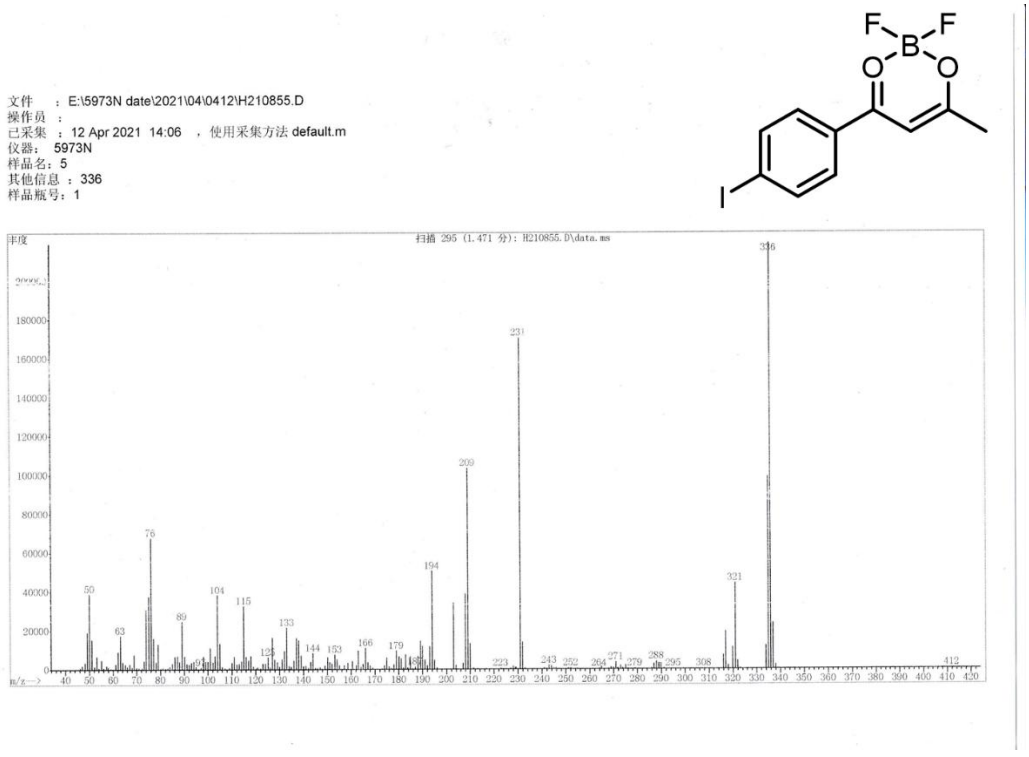

Figure S56. LRMS spectrum of IBF_2

National Center for Organic Mass Spectrometry in Shanghai
Shanghai Institute of Organic Chemistry
Chinese Academic of Sciences
High Resolution FI-MS Report
Low Resolution FI-MS Report

Instrument: JEOL-AccuTOF-GCv4G-GCT MS

Operation Mode: FI Positive Ion Mode (Counter Electrode: 10000V)

Card Serial Number: GCT-FI-T21-04-1490

Sample Serial Number: 2020274-5

Operator: Li Date: 2021/04/18

m/z	Theo. Mass	Delta (ppm)	RDB equiv.	Composition
334.9663	334.9663	0.06	3.5	$C_8H_8N_2F_4I$
	334.9661	0.62	6.0	$C_{10}H_8O_2{}^{10}BF_2I$
	334.9665	-0.69	-2.5	$C_4H_{14}O_4N_2ClFI$
	334.9666	-0.80	13.5	$C_{14}H_2O_4N_2ClF_2$
	334.9666	-0.83	1.5	$C_7H_{11}ON{}^{10}BClF_2I$

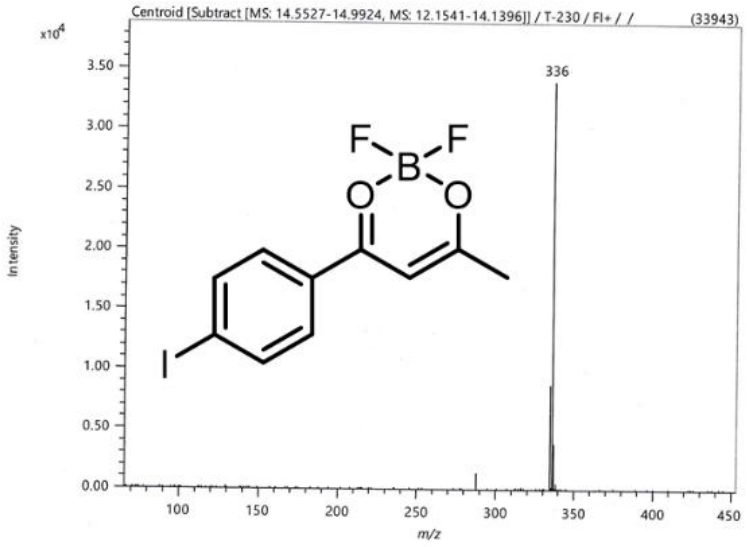

Figure S57. HRMS spectrum of IBF_2

Table S2. Crystal data and structure refinement for d8v21153.

Identification code	d8v21153	
Empirical formula	C10 H9 B F2 O2	
Formula weight	209.98	
Temperature	293(2) K	
Wavelength	0.71073 Å	
Crystal system	Orthorhombic	
Space group	P n m a	
Unit cell dimensions	a = 12.5443(6) Å	a= 90°.
	b = 7.1138(4) Å	b= 90°.
	c = 10.9392(7) Å	g = 90°.
Volume	976.19(10) $Å^3$	
Z	4	
Density (calculated)	1.429 Mg/m^3	
Absorption coefficient	0.121 mm^{-1}	
F(000)	432	
Crystal size	0.160 x 0.140 x 0.100 mm^3	
Theta range for data collection	3.248 to 25.980°.	
Index ranges	-15<=h<=15, -8<=k<=8, -13<=l<=13	
Reflections collected	8339	
Independent reflections	1030 [R(int) = 0.0292]	
Completeness to theta = 25.242°	99.1 %	
Absorption correction	Semi-empirical from equivalents	
Max. and min. transmission	0.7456 and 0.6726	
Refinement method	Full-matrix least-squares on F^2	
Data / restraints / parameters	1030 / 0 / 96	
Goodness-of-fit on F^2	1.069	
Final R indices [I>2sigma(I)]	R1 = 0.0384, wR2 = 0.1064	
R indices (all data)	R1 = 0.0471, wR2 = 0.1162	
Extinction coefficient	0.078(17)	
Largest diff. peak and hole	0.211 and -0.204 $e.Å^{-3}$	

Table S3. Atomic coordinates (x 10^4) and equivalent isotropic displacement parameters ($Å^2$x 10^3) for d8v21153. U(eq) is defined as one third of the trace of the orthogonalized U^{ij} tensor.

	x	y	z	U(eq)
F(1)	1589(1)	5928(1)	4027(1)	74(1)

O(1)	2623(1)	7500	2616(1)	64(1)
O(2)	3056(1)	7500	4794(1)	60(1)
C(1)	3922(2)	7500	1077(2)	66(1)
C(2)	3630(2)	7500	2391(2)	46(1)
C(3)	4374(1)	7500	3315(2)	46(1)
C(4)	4059(1)	7500	4514(2)	39(1)
C(5)	4795(1)	7500	5562(2)	40(1)
C(6)	4391(2)	7500	6739(2)	63(1)
C(7)	5071(2)	7500	7735(2)	72(1)
C(8)	6149(2)	7500	7564(2)	57(1)
C(9)	6563(2)	7500	6402(2)	51(1)
C(10)	5895(1)	7500	5406(2)	46(1)
B(1)	2190(2)	7500	3870(2)	51(1)

Table S4. Bond lengths [Å] and angles [°] for d8v21153.

F(1)-B(1)	1.3597(15)
O(1)-C(2)	1.287(2)
O(1)-B(1)	1.475(3)
O(2)-C(4)	1.295(2)
O(2)-B(1)	1.483(3)
C(1)-C(2)	1.483(3)
C(1)-H(1A)	0.93(2)
C(1)-H(1B)	0.97(4)
C(2)-C(3)	1.376(3)
C(3)-C(4)	1.370(2)
C(3)-H(3)	0.9300
C(4)-C(5)	1.472(2)
C(5)-C(6)	1.384(3)
C(5)-C(10)	1.391(2)
C(6)-C(7)	1.385(3)
C(6)-H(6)	0.9300
C(7)-C(8)	1.365(3)
C(7)-H(7)	0.9300
C(8)-C(9)	1.373(3)
C(8)-H(8)	0.9300
C(9)-C(10)	1.374(3)

C(9)-H(9)	0.9300
C(10)-H(10)	0.9300
B(1)-F(1)#1	1.3596(15)

C(2)-O(1)-B(1)	122.66(15)
C(4)-O(2)-B(1)	123.41(15)
C(2)-C(1)-H(1A)	107.7(13)
C(2)-C(1)-H(1B)	113.8(19)
H(1A)-C(1)-H(1B)	112.2(16)
O(1)-C(2)-C(3)	121.62(17)
O(1)-C(2)-C(1)	115.36(18)
C(3)-C(2)-C(1)	123.01(18)
C(4)-C(3)-C(2)	120.56(17)
C(4)-C(3)-H(3)	119.7
C(2)-C(3)-H(3)	119.7
O(2)-C(4)-C(3)	120.41(15)
O(2)-C(4)-C(5)	115.19(15)
C(3)-C(4)-C(5)	124.40(16)
C(6)-C(5)-C(10)	118.56(17)
C(6)-C(5)-C(4)	119.66(16)
C(10)-C(5)-C(4)	121.78(16)
C(5)-C(6)-C(7)	120.43(19)
C(5)-C(6)-H(6)	119.8
C(7)-C(6)-H(6)	119.8
C(8)-C(7)-C(6)	120.2(2)
C(8)-C(7)-H(7)	119.9
C(6)-C(7)-H(7)	119.9
C(7)-C(8)-C(9)	120.11(19)
C(7)-C(8)-H(8)	119.9
C(9)-C(8)-H(8)	119.9
C(8)-C(9)-C(10)	120.24(18)
C(8)-C(9)-H(9)	119.9
C(10)-C(9)-H(9)	119.9
C(9)-C(10)-C(5)	120.48(17)
C(9)-C(10)-H(10)	119.8
C(5)-C(10)-H(10)	119.8
F(1)#1-B(1)-F(1)	110.69(17)
F(1)#1-B(1)-O(1)	108.76(12)

F(1)-B(1)-O(1)	108.76(12)
F(1)#1-B(1)-O(2)	108.66(12)
F(1)-B(1)-O(2)	108.66(12)
O(1)-B(1)-O(2)	111.34(15)

Symmetry transformations used to generate equivalent atoms:

#1 x,-y+3/2,z

Table S5. Crystal data and structure refinement for mo_d8v20839_0m.

Identification code	mo_d8v20839_0m	
Empirical formula	C10 H8 B F2 I O2	
Formula weight	335.87	
Temperature	293(2) K	
Wavelength	0.71073 Å	
Crystal system	Monoclinic	
Space group	P 21/n	
Unit cell dimensions	a = 7.6012(3) Å	a= 90°.
	b = 14.2747(5) Å	b= 91.8010(10)°.
	c = 10.6115(4) Å	g = 90°.
Volume	1150.83(7) $Å^3$	
Z	4	
Density (calculated)	1.939 Mg/m^3	
Absorption coefficient	2.789 mm^{-1}	
F(000)	640	
Crystal size	0.200 x 0.160 x 0.130 mm^3	
Theta range for data collection	2.392 to 25.999°.	
Index ranges	-9<=h<=9, -17<=k<=17, -13<=l<=13	
Reflections collected	15738	
Independent reflections	2235 [R(int) = 0.0494]	
Completeness to theta = 25.242°	98.7 %	
Absorption correction	Semi-empirical from equivalents	
Max. and min. transmission	0.7456 and 0.4111	
Refinement method	Full-matrix least-squares on F^2	
Data / restraints / parameters	2235 / 0 / 147	
Goodness-of-fit on F^2	1.071	
Final R indices [I>2sigma(I)]	R1 = 0.0296, wR2 = 0.0780	
R indices (all data)	R1 = 0.0318, wR2 = 0.0798	
Extinction coefficient	0.0151(17)	
Largest diff. peak and hole	1.001 and -0.586 $e.Å^{-3}$	

Table S6. Atomic coordinates (x 10^4) and equivalent isotropic displacement parameters ($Å^2$x 10^3) for mo_d8v20839_0m. U(eq) is defined as one third of the trace of the orthogonalized U^{ij} tensor.

	x	y	z	U(eq)
I(1)	8175(1)	3443(1)	8477(1)	58(1)
F(1)	5421(4)	8027(2)	3294(2)	74(1)
F(2)	8303(4)	8371(2)	3103(3)	77(1)
O(1)	6992(3)	7308(2)	1715(2)	47(1)
O(2)	7517(3)	6952(2)	3954(2)	47(1)
C(1)	7083(4)	4498(2)	4701(3)	43(1)
C(2)	7257(5)	3924(2)	5756(3)	46(1)
C(3)	7956(4)	4285(2)	6866(3)	39(1)
C(4)	8489(5)	5209(2)	6950(3)	45(1)
C(5)	8302(4)	5782(2)	5907(3)	40(1)
C(6)	7587(4)	5434(2)	4773(3)	34(1)
C(7)	7339(4)	6063(2)	3694(3)	35(1)
C(8)	6983(4)	5769(2)	2468(3)	41(1)
C(9)	6893(4)	6421(2)	1502(3)	40(1)
C(10)	6753(5)	6151(3)	155(3)	54(1)
B(1)	7055(6)	7695(3)	3024(4)	48(1)

Table S7. Bond lengths [Å] and angles [°] for mo_d8v20839_0m.

I(1)-C(3)	2.092(3)
F(1)-B(1)	1.368(5)
F(2)-B(1)	1.353(5)
O(1)-C(9)	1.289(4)
O(1)-B(1)	1.494(4)
O(2)-C(7)	1.304(4)
O(2)-B(1)	1.484(4)
C(1)-C(2)	1.390(5)
C(1)-C(6)	1.391(4)
C(1)-H(1)	0.9300
C(2)-C(3)	1.377(5)
C(2)-H(2)	0.9300
C(3)-C(4)	1.382(4)

C(4)-C(5)	1.380(4)
C(4)-H(4)	0.9300
C(5)-C(6)	1.395(4)
C(5)-H(5)	0.9300
C(6)-C(7)	1.463(4)
C(7)-C(8)	1.385(4)
C(8)-C(9)	1.384(4)
C(8)-H(8)	0.9300
C(9)-C(10)	1.482(4)
C(10)-H(10A)	0.9600
C(10)-H(10B)	0.9600
C(10)-H(10C)	0.9600

C(9)-O(1)-B(1)	121.8(2)
C(7)-O(2)-B(1)	122.3(2)
C(2)-C(1)-C(6)	120.2(3)
C(2)-C(1)-H(1)	119.9
C(6)-C(1)-H(1)	119.9
C(3)-C(2)-C(1)	119.5(3)
C(3)-C(2)-H(2)	120.3
C(1)-C(2)-H(2)	120.3
C(2)-C(3)-C(4)	121.1(3)
C(2)-C(3)-I(1)	120.2(2)
C(4)-C(3)-I(1)	118.7(2)
C(5)-C(4)-C(3)	119.4(3)
C(5)-C(4)-H(4)	120.3
C(3)-C(4)-H(4)	120.3
C(4)-C(5)-C(6)	120.5(3)
C(4)-C(5)-H(5)	119.7
C(6)-C(5)-H(5)	119.7
C(1)-C(6)-C(5)	119.2(3)
C(1)-C(6)-C(7)	121.2(3)
C(5)-C(6)-C(7)	119.6(3)
O(2)-C(7)-C(8)	120.6(3)
O(2)-C(7)-C(6)	114.9(2)
C(8)-C(7)-C(6)	124.4(3)
C(9)-C(8)-C(7)	119.7(3)
C(9)-C(8)-H(8)	120.1

C(7)-C(8)-H(8)	120.1
O(1)-C(9)-C(8)	122.0(3)
O(1)-C(9)-C(10)	115.3(3)
C(8)-C(9)-C(10)	122.7(3)
C(9)-C(10)-H(10A)	109.5
C(9)-C(10)-H(10B)	109.5
H(10A)-C(10)-H(10B)	109.5
C(9)-C(10)-H(10C)	109.5
H(10A)-C(10)-H(10C)	109.5
H(10B)-C(10)-H(10C)	109.5
F(2)-B(1)-F(1)	112.3(3)
F(2)-B(1)-O(2)	108.5(3)
F(1)-B(1)-O(2)	107.8(3)
F(2)-B(1)-O(1)	108.9(3)
F(1)-B(1)-O(1)	108.6(3)
O(2)-B(1)-O(1)	110.7(3)

Symmetry transformations used to generate equivalent atoms:

References

1. Fermi, G. Bergamini, R. Peresutti, E. Marchi, M. Roy, P. Ceroni, M. Gingras, *Dyes Pigments.* 2014, **110**, 113.
2. L. Xu, G. Li, T. Xu, W. Zhang, S. Zhang, S. Yin, Z. An, G. He, *Chem. Commun.* 2018, **54**, 9226.
3. Bolton, K. Lee, H. J. Kim, K. Y. Lin, J. Kim, *Nat. Chem.* 2011, **3**, 205.
4. Z. Y. Zhang, Y. Chen, Y. Liu, *Angew. Chem. Int. Ed.* 2019, **58**, 6028.
5. L. Xiao, Y. Wu, J. Chen, Z. Yu, Y. Liu, J. Yao, H. Fu, *J. Phys. Chem. A* 2017, **121**, 8652.
6. S. Xu, W. Wang, H. Li, J. Zhang, R. Chen, S. Wang, C. Zheng, G. Xing, C. Song, W. Huang, *Nat. Commun.* 2020, **11**, 4802.
7. Z. Yang, C. Xu, W. Li, Z. Mao, X. Ge, Q. Huang, H. Deng, J. Zhao, F. L. Gu, Y. Zhang, Z. Chi, *Angew. Chem. Int. Ed.* 2020, **59**, 17451.
8. W. Zhao, T. S. Cheung, N. Jiang, W. Huang, J. W. Y. Lam, X. Zhang, Z. He, B. Z. Tang, *Nat. Commun.* 2019, **10**, 1595.
9. H. Shi, L. Song, H. Ma, C. Sun, K. Huang, A. Lv, W. Ye, H. Wang, S. Cai, W. Yao, Y. Zhang, R. Zheng, Z. An, W. Huang, *J. Phys. Chem. Lett.* 2019, **10**, 595.
10. Z. Yin, M. Gu, H. Ma, X. Jiang, J. Zhi, Y. Wang, H. Yang, W. Zhu, Z. An, *Angew. Chem. Int. Ed.* 2021, **60**, 2058.
11. P. Xue, P. Wang, P. Chen, B. Yao, P. Gong, J. Sun, Z. Zhang, R. Lu, *Chem. Sci.* 2017, **8**, 6060.
12. J. Jin, H. Jiang, Q. Yang, L. Tang, Y. Tao, Y. Li, R. Chen, C. Zheng, Q. Fan, K. Y. Zhang, Q. Zhao, W. Huang, *Nat. Commun.* 2020, **11**, 842.

13. Bhattacharjee, S. Hirata, *Adv. Mater.* 2020, **32**, 2001348.
14. X. Liu, W. Dai, J. Qian, Y. Lei, M. Liu, Z. Cai, X. Huang, H. Wu, Y. Dong, *J. Mater. Chem. C* 2021, **9**, 3391.
15. X. Wang, Y. Sun, G. Wang, J. Li, X. Li, K. Zhang, *Angew. Chem. Int. Ed.* 2021, **26**, 17138.
16. Y. Wen, H. Liu, S. Zhang, Y. Gao, Y. Yan, B. Yang, *J. Mater. Chem. C* 2019, **7**, 12502.
17. L. Gu, H. Wu, H. Ma, W. Ye, W. Jia, H. Wang, H. Chen, N. Zhang, D. Wang, C. Qian, Z. An, W. Huang, Y. Zhao, *Nat. Commun.* 2020, **11**, 944.
18. W. Z. Yuan, X. Y. Shen, H. Zhao, J. W. Y. Lam, L. Tang, P. Lu, C. Wang, Y. Liu, Z. Wang, Q. Zheng, J. Z. Sun, Y. Ma, B. Z. Tang, *J. Phys. Chem. C* 2010**, 114***,* 6090.
19. J. Wang, C. Wang, Y. Gong, Q. Liao, M. Han, T. Jiang, Q. Dang, Y. Li, Q. Li, Z. Li, *Angew. Chem. Int. Ed.* 2018, **57**, 16821
20. J. Wang, X. Gu, H. Ma, Q. Peng, X. Huang, X. Zheng, S. H. P. Sung, G. Shan, J. W. Y. Lam, Z. Shuai, B. Z. Tang, *Nat. Commun.* 2018, **9**, 2963.
21. M. Villa, B. D. Secco, L. Ravotto, M. Roy, E. Rampazzo, N. Zaccheroni, L. Prodi, M. Gingras, S. A. Vinogradov, P. Ceroni, *J. Phys. Chem. C* 2019, **123**, 29884.
22. H. Wu, C. Hang, X. Li, L. Yin, M. Zhu, J. Zhang, Y. Zhou, H. Agren, Q. Zhang, L. Zhu, *Chem. Commun.* 2017, **53**, 2661.
23. H. Wu, Y. Zhou, L. Yin, C. Hang, X. Li, H. Agren, T. Yi, Q. Zhang, L. Zhu, *J. Am. Chem. Soc.* 2017, **139**, 2, 785.
24. Z. Mao, Z. Yang, Y. Mu, Y. Zhang, Y.-F. Wang, Z. Chi, C.-C. Lo, S. Liu, A. Lien, J. Xu, *Angew. Chem. Int. Ed.* 2015, **54**, 6270.
25. Y. Gong, G. Chen, Q. Peng, W. Z. Yuan, Y. Xie, S. Li, Y. Zhang, B. Z. Tang, *Adv. Mater.* 2015, **27**, 6195.
26. S. Cai, H. Shi, J. Li, L. Gu, Y. Ni, Z. Cheng, S. Wang, W. Xiong, L. Li, Z. An, W. Huang, *Adv. Mater.* 2017, **29**, 1701244.
27. Z. Yang, Z. Mao, X. Zhang, D. Ou, Y. Mu, Y. Zhang, C. Zhao, S. Liu, Z. Chi, J. Xu, Y.-C. Wu, P.-Y. Lu, A. Lien, M. R. Bryce, *Angew. Chem. Int. Ed.* 2016, **55**, 2181.
28. S. M. A. Fateminia, Z. Mao, S. Xu, Z. Yang, Z. Chi, B. Liu, *Angew. Chem. Int. Ed.* 2017, **56**, 12160.
29. G. Zhang, G. M. Palmer, M. W. Dewhirst, C. L. Fraser, *Nat. Mater.* **2009**, 8, 747.
30. Z.-Y. Zhang, Y. Liu, *Chem. Sci.* 2019, **10**, 7773.
31. X.-K. Ma, W. Zhang, Z. Liu, H. Zhang, B. Zhang, Y. Liu, *Adv. Mater.* 2021, 2007476.
32. M. S. Kwon, Y. Yu, C. Coburn, A. W. Phillips, K. Chung, A. Shanker, J. Jung, G. Kim, K. Pipe, S. R. Forrest, J. H. Youk, J. Gierschner, J. Kim, *Nat. Commun.* 2015, **6**, 8947.
33. J. A. Li, J. Zhou, Z. Mao, Z. Xie, Z. Yang, B. Xu, C. Liu, X. Chen, D. Ren, H. Pan, G. Shi, Y. Zhang, Z. Chi, *Angew. Chem. Int. Ed.* 2018, **57**, 6449.
34. S. Xu, R. Chen, C. Zheng, W. Huang, *Adv. Mater.* 2016, **28**, 9920.
35. J. Wei, B. Liang, R. Duan, Z. Cheng, C. Li, T. Zhou, Y. Yi, Y. Wang, *Angew. Chem. Int. Ed.* 2016, **55**, 15589.
36. J. Yang, X. Zhen, B. Wang, X. Gao, Z. Ren, J. Wang, Y. Xie, J. Li, Q. Peng, K. Pu, Z. Li, *Nat. Commun.* 2018, **9**, 840.
37. E. Lucenti, A. Forni, C. Botta, L. Carlucci, C. Giannini, D. Marinotto, A. Pavanello, A. Previtali, S. Righetto, E. Cariati, *Angew. Chem. Int. Ed.* 2017, **56**, 16302.
38. X. F. Wang, H. Xiao, P. Z. Chen, Q. Z. Yang, B. Chen, C. H. Tung, Y. Z. Chen, L. Z. Wu, *J.*

Am. Chem. Soc. 2019, **141**, 5045.
39. W. Zhao, T. S. Cheung, N. Jiang, W. Huang, J. W. Y. Lam, X. Zhang, Z. He, B. Z. Tang, *Nat. Commun.* 2019, **10**, 1595.
40. T. Zhang, C. Wang, X. Ma, Ind. Eng. *Chem. Res.* 2019, **58**, 7778.
41. B. Li, Y. Gong, L. Wang, H. Lin, Q. Li, F. Guo, Z. Li, Q. Peng, Z. Shuai, L. Zhao, Y. Zhang, *J. Phys. Chem. Lett.* 2019, **10**, 7141.
42. J. Yuan, R. Chen, X. Tang, Y. Tao, S. Xu, L. Jin, C. Chen, X. Zhou, C. Zheng, W. Huang, *Chem. Sci.* 2019, **10**, 5031.
43. H. Ma, A. Lv, L. Fu, S. Wang, Z. An, H. Shi, W. Huang, *Ann. Phys.* (Berlin) 2019, **531**, 1800482.
44. X. Ma, J. Cao, Q. Wang, H. Tian, *Chem. Commun.* 2011, **47**, 3559.
45. H. Shi, L. Zou, K. Huang, H. Wang, C. Sun, S. Wang, H. Ma, Y. He, J. Wang, H. Yu, W. Yao, Z. An, Q. Zhao, W. Huang, *ACS Appl. Mater. Interfaces* 2019, **11**, 18103.
46. D. Liu, A. M. El-Zohry, M. Taddei, C. Matt, L. Bussotti, Z. Wang, J. Zhao, O. F. Mohammed, M. D. Donato, S. Weber, *Angew. Chem. Int. Ed.* 2020, **59**, 11591.
47. P. She, Y. Yu, Y. Qin, Y. Zhang, F. Li, Y. Ma, S. Liu, W. Huang, Q. Zhao, *Adv. Optical Mater.* 2020, **8**, 1901437.
48. X.-N. Li, M. Yang, X.-L. Chen, J.-H. Jia, W.-W. Zhao, X.-Y. Wu, S.-S. Wang, L. Meng, C.-Z. Lu, *Small* 2019, **15**, 1903270.
49. D. R. Lee, K. H. Lee, W. Shao, C. L. Kim, J. Kim, J. Y. Lee, *Chem. Mater.* 2020, **32**, 2583.
50. X. Chen, C. Xu, T. Wang, C. Zhou, J. Du, Z. Wang, H. Xu, T. Xie, G. Bi, J. Jiang, X. Zhang, J. N. Demas, C. O. Trindle, Y. Luo, G. Zhang, *Angew. Chem. Int. Ed.* 2016, **55**, 9872.
51. H. Chen, X. Yao, X. Ma, H. Tian, *Adv. Optical Mater.* 2016, **4**, 1397.
52. S. Cai, H. Shi, D. Tian, H. Ma, Z. Cheng, Q. Wu, M. Gu, L. Huang, Z. An, Q. Peng, W. Huang, *Adv. Funct. Mater.* 2018, **28**, 1705045.
53. A. Fermi, G. Bergamini, M. Roy, M. Gingras, P. Ceroni, *J. Am. Chem. Soc.* 2014, **136**, 6395.
54. Z. He, W. Zhao, J. W. Y. Lam, Q. Peng, H. Ma, G. Liang, Z. Shuai, B. Z. Tang, *Nat. Commun.* 2017, **8**, 416.
55. G. He, W. T. Delgado, D. J. Schatz, C. Merten, A. Mohammadpour, L. Mayr, M. J. Ferguson, R. McDonald, A. Brown, K. Shankar, E. Rivard, *Angew. Chem. Int. Ed.* 2014, **53**, 4587.
56. K. Kanosue, S. Hirata, M. Vacha, R. Augulis, V. Gulbinas, R. Ishige, S. Ando, *Mater. Chem. Front.* 2019, **3**, 39.
57. S. Hirata, *Adv. Sci.* 2019, **6**, 1900410.
58. W. T. Delgado, C. A. Braun, M. P. Boone, O. Shynkaruk, Y. Qi, R. McDonald, M. J. Ferguson, P. Data, S. K. C. Almeida, I. de Aguiar, G. L. C. de Souza, A. Brown, G. He, E. Rivard, *ACS Appl. Mater. Interfaces* 2018, 10, **15**, 12124.
59. Q. J. Shen, H. Q. Wei, W. S. Zou, H. L. Sun, W. J. Jin, *CrystEngComm* 2012, **14**, 1010.
60. M. S. Kwon, D. Lee, S. Seo, J. Jung, J. Kim, *Angew. Chem.* 2014, **126**, 11359.